

Microscopic Description of Critical Bubbles

Carlos Hoyos,^{1,2} David Mateos,^{3,4,5}

Wilke van der Schee,^{6,7,8} Javier G. Subils⁶

¹ Departamento de Física, Universidad de Oviedo,

Calle Leopoldo Calvo Sotelo 18, ES-33007, Oviedo, Spain.

² Instituto Universitario de Ciencias y Tecnologías Espaciales de Asturias (ICTEA),
Calle de la Independencia 13, ES-33004, Oviedo, Spain.

³ Departament de Física Quàntica i Astrofísica & Institut de Ciències del Cosmos (ICC),
Universitat de Barcelona, Martí i Franquès 1, ES-08028, Barcelona, Spain.

⁵ Institució Catalana de Recerca i Estudis Avançats (ICREA),
Passeig Lluís Companys 23, ES-08010, Barcelona, Spain.

⁶ Institute for Theoretical Physics, Utrecht University, 3584 CC Utrecht, The Netherlands.

⁷ Theoretical Physics Department, CERN CH-1211 Genève 23, Switzerland.

⁸ Nikhef, Science Park 105, 1098 XG Amsterdam, The Netherlands.

Abstract

First-order phase transitions occur through the nucleation of critical bubbles of the stable phase within the metastable phase. Using holography, we present a fully microscopic description of these bubbles in a strongly coupled, four-dimensional gauge theory at finite temperature. In the gravitational dual, these bubbles correspond to static, inhomogeneous and unstable black-brane solutions with a localized deformation on the horizon. We construct these solutions across the entire metastable branch and compute the surface tension and the nucleation rate. We then compare these microscopic results with those obtained from a two-derivative effective action for the order parameter in two different scenarios. When the effective action is derived from the microscopic theory via holography, we find remarkable agreement. However, when the effective action is constrained only by the equation of state and dimensional analysis, significant discrepancies emerge. These discrepancies can be resolved if an additional constraint related to the surface tension is imposed.

Contents

1	Introduction	2
2	Holographic set-up	5
2.1	Model	5
2.2	Homogeneous solutions	6
2.3	Inhomogeneous solutions	7
2.4	Thermodynamics	10
3	Results	13
3.1	Phase diagram	13
3.2	Critical bubbles	16
3.3	Nucleation rate	19
4	Effective description	20
4.1	Definition of the effective action	21
4.2	Holographic construction of the effective action	24
4.3	Phenomenological construction of the effective action	28
5	Conclusions	33
A	Numerical Implementation	34
B	Holographic Renormalization	37
C	Free energy	39
C.1	Useful expressions	39
C.2	Evaluation of the on-shell action	40
D	Calculation of the two-point function	42

1 Introduction

First-order phase transitions (FOPT) are a ubiquitous phenomenon across physics. They play a central role in a wide range of systems, from condensed matter to high-energy contexts. In cosmology, for instance, FOPT may occur during the early universe in many scenarios that extend the Standard Model [1–5] (see [6] for a recent review). This has potential consequences for baryogenesis [7–11], gravitational wave production [12–20], and cosmic defect formation [2, 21–25]. In astrophysics, they are relevant to the physics of dense QCD matter in core collapse supernovae [26–31] or in neutron stars (mergers) [32–41]. In all these settings, the dynamics of the transition is governed by a relativistic Quantum Field Theory (QFT) at finite temperature.

A key feature of FOPT is the nucleation of critical bubbles of the stable phase within a metastable background. These bubbles are intrinsically nonperturbative objects whose

properties govern important aspects of the transition dynamics and its observable consequences. The free energy of the critical bubbles determines the nucleation rate, which in turn influences the duration and completion of the phase transition [42, 43]. The bubble wall profile, describing the spatial variation of the order parameter and other fields across the bubble interface, plays a crucial role in scenarios where baryogenesis occurs through a FOPT, by controlling the necessary CP-violating and out-of-equilibrium effects [44–46]. Understanding these microscopic features is therefore essential for a precise modeling of the phenomenology of FOPTs.

In most applications, the critical bubbles are studied using an effective field theory (EFT) description for the order parameter, which is usually assumed to be a single scalar field. While this approach can provide powerful insights, it relies on the validity of a derivative expansion that may not hold if gradients become large, as expected at the bubble wall. In addition, in many cases of interest the effective action cannot be determined from first principles. In some instances, this is because the microscopic theory is unknown, as in Beyond the Standard Model scenarios. In other cases, the microscopic theory is known, but calculating the effective action from first principles is not feasible due to technical challenges, such as the strongly coupled nature of the physics. Under these circumstances, one can still attempt to construct an effective action motivated by a combination of phenomenological considerations and dimensional analysis. To assess the regime of validity of these approximations, a fully microscopic description of the critical bubbles is necessary. This requires a nonperturbative treatment of the underlying QFT, regardless of whether the theory is weakly or strongly coupled.

In this work, we pursue such a microscopic approach using holography, which provides a framework for studying large- N , strongly coupled gauge theories via a dual gravitational description in higher dimensions [47–49]. In particular, thermal phase transitions in the boundary theory correspond to transitions between black brane geometries in the bulk. This approach has been successfully used to assess the validity of hydrodynamics [50–57], to simulate the real-time dynamics of a phase transition [58–64], to determine the velocity with which supercritical bubbles expand [65–68], to compute the corresponding gravitational wave spectrum [63, 69], and to find the effective action for the order parameter [70, 71].

Ref. [67] provided an approximate microscopic description of critical bubbles by fine-tuning the initial conditions in a time-dependent set-up. More recently, the problem has been investigated in the probe approximation, in which only a small subset of degrees of freedom undergo the FOPT, with the goal of testing the effective approach [72], finding good agreement. In contrast, here we construct fully backreacted, exact duals of critical bubbles as static, inhomogeneous, and unstable black-brane solutions featuring localized deformations along the horizon—see Fig. 1. This approach allows us to compute the properties of the bubbles directly from the microscopic theory. We then compare these properties to those obtained from a two-derivative effective action for the order parameter in two different scenarios. In the first one, we use holography to derive the effective action from first principles. In this case we find remarkable agreement with the microscopic results. In the second scenario, we simply model the effective potential as a degree-four

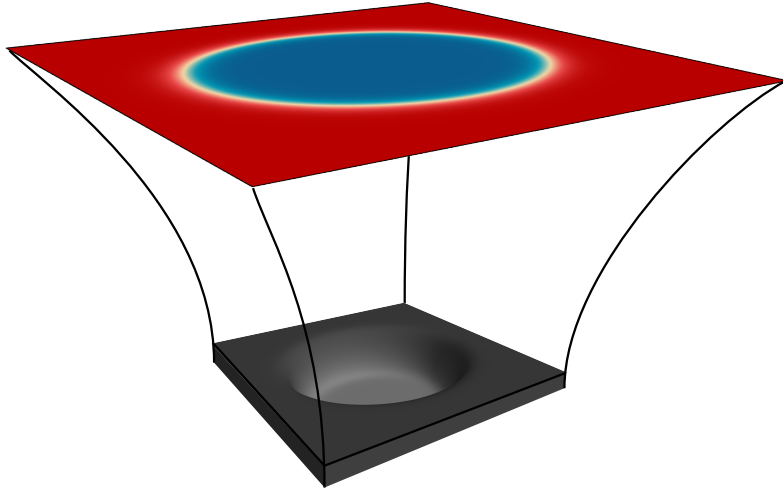


Figure 1: A critical bubble (top part of the figure) is dual to an inhomogeneous static black brane geometry (bottom part).

polynomial, determined by the equation of state, and fix the coefficient of the kinetic term using dimensional analysis. This approach significantly overestimates the magnitude of this coefficient, leading to substantial discrepancies with the microscopic results. Ultimately, these discrepancies can be traced to a suppression of the surface tension relative to the naive dimensional estimate. By adjusting the kinetic term in the effective action to ensure that the correct surface tension is reproduced, we restore agreement with the microscopic results.

Our results provide new insights into the microscopic structure of phase transitions in strongly coupled systems, offering a controlled framework for testing and extending the applicability of effective models. The strong interactions suggest parallels with FOPT in pure $SU(N)$ Yang-Mills (YM) theories with $N > 2$. While we will comment on these similarities below, it is important to interpret this comparison with caution, as, unlike in YM theories, the FOPT in our case occurs between two plasma-like, deconfined phases.

In this paper we will focus on so-called $O(3)$ -symmetric bubbles, namely, those nucleated mostly through thermal fluctuations, as opposed to $O(4)$ -symmetric bubbles nucleated mostly through quantum effects. In our case, it is plausible that the former dominate the nucleation because the metastable branch does not extend to parametrically small temperatures. Since $O(3)$ -symmetric bubbles are independent of the Euclidean-time direction, we will find them directly as static Lorentzian solutions, which should be thought of as initial conditions for the post-nucleation Lorentzian-time evolution.

The paper is organized as follows. In Section 2 we introduce the model, present its main properties, and explain how to construct homogeneous and inhomogeneous phases. In Section 3 we present our results for the critical bubbles at different temperatures. In Section 4 we investigate if it is possible to obtain similar results from an effective approach. We conclude and discuss future directions in Section 5. Technical details of our computations and numerical implementation are relegated to Appendices A, B, C and D.

2 Holographic set-up

2.1 Model

Our gravitational bulk theory is described by the Einstein-dilaton action

$$I_g = \frac{2}{\kappa_5^2} \int d^5x \sqrt{-G} \left(\frac{R}{4} - \frac{1}{2} \partial_M \phi \partial^M \phi - V(\phi) \right), \quad (2.1)$$

with G the determinant of the five-dimensional spacetime metric G_{MN} and R its Ricci scalar. We assume that the potential $V(\phi)$ can be written in terms of a superpotential $W(\phi)$ through the standard relation

$$V(\phi) = -\frac{4}{3}W(\phi)^2 + \frac{1}{2} \left(\frac{\partial W(\phi)}{\partial \phi} \right)^2. \quad (2.2)$$

This choice does not imply that the theory is supersymmetric but it is simply a convenient way to specify the actual potential. We take the superpotential to lie in the class of models introduced in [73]:

$$W(\phi) = \frac{1}{L} \left(-\frac{3}{2} - \frac{\phi^2}{2} + \lambda_4 \phi^4 + \lambda_6 \phi^6 \right), \quad (2.3)$$

where L is the asymptotic AdS radius, $\lambda_4 = -1/4$ and $\lambda_6 = 1/10$. In the notation of Refs. [63, 65, 67, 74], these choices correspond to $\phi_M = 1, \phi_Q = 10$, and are motivated by the fact that they give rise to a simple bulk theory dual to a four-dimensional gauge theory with a first-order phase transition. More details can be found in Ref. [73].

The potential has a maximum at the origin, where the system admits as a solution AdS space with radius L . This solution is dual to a 3+1 dimensional conformal field theory (CFT). The potential approaches the maximum as

$$V(\phi) = \frac{1}{L^2} \left(-3 - \frac{3}{2} \phi^2 - \frac{\phi^4}{3} + O(\phi^6) \right). \quad (2.4)$$

In particular, the mass of ϕ around $\phi = 0$ is $m^2 L^2 = -3$, which means that solutions with nontrivial profiles for this scalar field describe deformations of the CFT by a dimension-three scalar operator \mathcal{O} , dual to ϕ . In addition, for our choice of parameters λ_4 and λ_6 , the potential and the superpotential have a minimum at

$$\phi_{\text{IR}}^2 = -\frac{\lambda_4}{3\lambda_6} + \frac{\sqrt{4\lambda_4^2 + 6\lambda_6}}{6\lambda_6}, \quad (2.5)$$

where AdS with radius $L_{\text{IR}} = \sqrt{-3/V(\phi_{\text{IR}})}$ is again an exact solution, dual to an IR CFT to which the deformed UV theory flows. For different values of the parameters additional extrema can appear, leading to interesting dynamics [73].

Finite-temperature states in the gauge theory are dual in the bulk to solutions with a horizon. We will discuss how to find these in the rest of this section. In Section 2.2 we focus on homogeneous phases, described by homogeneous black brane solutions. We know from previous work that some of these will be metastable or unstable and lead to the

development of inhomogeneities. In Section 2.3 we will exploit this feature to find static inhomogeneous solutions with spherical symmetry in the gauge theory directions, which we will interpret as critical bubbles. Then in Section 2.4 we explain how to extract their thermodynamic properties.

2.2 Homogeneous solutions

Homogeneous, finite-temperature states in the gauge theory correspond to bulk solutions with a homogeneous horizon. We will construct these solutions in this section. In addition to allowing us to determine the phase diagram of the theory, these solutions will later provide a seed for the construction of their inhomogeneous counterparts.

A convenient ansatz to find homogeneous black brane solutions is

$$ds^2 = \frac{L^2}{z^2} \left[-f(z)dt^2 + g(z) \left(d\rho^2 + \rho^2 d\Omega_{(2)} \right) + dz^2 \right], \quad (2.6)$$

with $f(z), g(z)$ functions of the holographic coordinate to be determined, and

$$d\Omega_{(2)} = d\theta_1^2 + \sin^2 \theta_1 d\theta_2^2 \quad (2.7)$$

the line element of a two-dimensional sphere. The boundary is located at $z = 0$. The scalar ϕ is also chosen to depend only on the holographic coordinate, namely:

$$\phi = \psi(z). \quad (2.8)$$

The metric in Eq. (2.6) is of the form

$$ds^2 = \frac{L^2}{\tilde{z}^2} \left(d\tilde{z}^2 + g_{\mu\nu}(\tilde{z}, x) dx^\mu dx^\nu \right) \quad (2.9)$$

with $\tilde{z} = z$, which, in particular, has $G_{\mu\tilde{z}} = 0$, and is thus written in Fefferman-Graham (FG) coordinates. The condition for a regular horizon at some position $z = z_H$ is that $f(z)$ has a double zero and that the rest of the functions are finite:

$$f(z) = f_H(z - z_H)^2 + \dots, \quad g(z) = g_H + \dots, \quad \psi(z) = \phi_H + \dots. \quad (2.10)$$

For later purposes, note that f_H has dimensions of mass squared. We can use this series expansion to seed a numerical integrator such as Mathematica `NDSolve` to find the different profiles for the functions all the way up to the boundary at $z = 0$, where the metric asymptotes to pure AdS. In this limit, the functions f and g approach constant values, which can be set to one taking advantage of the three independent rescaling symmetries (see Ref. [75] for details)

$$g \rightarrow \mu_g^2 g, \quad f \rightarrow \mu_f^2 f, \quad z \rightarrow \mu_z z. \quad (2.11)$$

With this choice, the expansions near the boundary become

$$\begin{aligned} \psi(z) &= \phi_s z + v z^3 + O(z^5), \\ f(z) &= 1 - \frac{\phi_s^2}{3} z^2 + f_4 z^4 + O(z^6), \\ g(z) &= 1 - \frac{\phi_s^2}{3} z^2 + \frac{1}{27} \left[2 \left(\phi_s^4 - 9 \phi_s v \right) - 9 f_4 \right] z^4 + O(z^6). \end{aligned} \quad (2.12)$$

The coefficient ϕ_s in the leading fall-off of the scalar has dimensions of mass. In the dual boundary theory it plays the role of a coupling or source for the scalar operator \mathcal{O} dual to ϕ . In general, a solution with a given value of ϕ_s corresponds to a theory with a coupling Λ responsible for the breaking of conformal invariance, and a constant source J , in such a way that $\phi_s = \Lambda + J$. We split ϕ_s in this way because we will think of Λ as the scale defining a given theory, and of J as a quantity that we introduce in order to compute the generating functional of correlation functions of \mathcal{O} in that theory. We will set $J = 0$ until Section 4, where we will reintroduce J in order to compute the effective action. The expressions for non-zero J can be obtained by replacing $\Lambda \rightarrow \Lambda + J$ in all the formulas below. We will see below that the coefficient of the subleading term, v , is related to the expectation value of \mathcal{O} . Similarly, the coefficient f_4 is related to the energy density and the pressures in the gauge theory.

The first rescaling in (2.11) implies that there is a radially conserved quantity

$$Q \equiv \frac{L^3}{z^3} \sqrt{\frac{g(z)}{f(z)}} [g(z)f'(z) - f(z)g'(z)], \quad (2.13)$$

meaning that $\partial_z Q = 0$.¹ This radial conservation law may be used to partially relate UV and IR quantities. More precisely, Q can be expressed in terms of f_4 , Λ and v using the UV expansions in Eq. (2.12), while evaluating Q using the IR asymptotics in Eq. (2.10) allows us to express it in terms of f_H and g_H . From this we conclude that

$$f_4 = -\frac{3f_H^{\frac{1}{2}}g_H^{\frac{3}{2}}}{8z_H^3} + \frac{1}{18}(\Lambda^4 - 9\Lambda v). \quad (2.14)$$

2.3 Inhomogeneous solutions

Our goal in this section is to construct inhomogeneous solutions corresponding to critical bubbles in the gauge theory. In the gauge theory, these configurations are spherically symmetric and hence their profile depends only on the radial direction ρ . The corresponding solutions in the bulk will depend on ρ and on the holographic coordinate z .

To construct inhomogeneous solutions, we use DeTurck's trick, see Refs. [76–78]. This is a useful procedure to fix the gauge in such a way that Einstein's equations are elliptic. The trick relies on choosing a reference metric \bar{G}_{MN} which behaves near the boundary as the metric we are seeking, G_{MN} . Then one defines the *DeTurck vector*,

$$\xi^P = G^{MN}(\Gamma_{MN}^P - \bar{\Gamma}_{MN}^P), \quad (2.15)$$

where Γ_{MN}^P and $\bar{\Gamma}_{MN}^P$ are the Christoffel symbols of the metrics G_{MN} and \bar{G}_{MN} , respectively. We then look for solutions to

$$R_{MN} - \frac{R}{2}G_{MN} - \left(\nabla_{(M}\xi_{N)} - \frac{1}{2}\nabla_A\xi^A G_{MN} \right) = T_{MN}, \quad (2.16)$$

where T_{MN} is the stress tensor of the scalar field. When $\xi = 0$, Eq. (2.16) reduces to the Einstein equations derived from Eq. (2.1). Potential solutions with $\xi \neq 0$ are called

¹In contrast, the conserved quantities under the other two rescalings are identically zero.

DeTurck solitons and it can be proven that they do not exist under certain conditions, see Refs. [79, 80]. Here, we monitor $\xi_A \xi^A$ and check that ξ_A vanishes in our solutions.

Let us now introduce our choice of reference metric \bar{G}_{MN} . A usual choice in this context is to use a black brane in pure AdS, which in terms of Eq. (2.6) reads

$$f(z) = 1 + \frac{z^4}{z_H^4} - \frac{4z^4}{z^4 + z_H^4}, \quad g(z) = 1 + \frac{z^4}{z_H^4}. \quad (2.17)$$

In our case we have made a different choice, because the solutions we seek will asymptote at large distances (at large values of ρ) to one of the homogeneous solutions constructed in Section 2.2, which differ from Eq. (2.17) because of the non-zero scalar field profile. The physical reason for this is that the bubble configuration is a localized perturbation within a given metastable solution. Consequently, for each choice of temperature, we take the homogeneous metastable solution at that temperature as the reference metric \bar{G}_{MN} . One may be concerned that this makes our reference metric already numerical. However, this will not pose a problem because we will be able to determine it with very high precision. Moreover, with this choice of reference metric all the components of the DeTurck vector except ξ^z and ξ^ρ vanish identically in Eq. (2.15). Then ξ^A is spacelike and $\xi^A \xi_A = 0$ if and only if $\xi^A = 0$.

To find inhomogeneous, spherically symmetric solutions we start with the following ansatz for the metric:

$$\begin{aligned} ds^2 = \frac{L^2}{z^2} \left[-f(z)Q_1(\rho, z)dt^2 + g(z) \left(Q_2(\rho, z)d\rho^2 + \rho^2 Q_3(\rho, z)d\Omega_{(2)} \right) \right. \\ \left. + Q_4(\rho, z)dz^2 + (z_H - z)Q_5(\rho, z)d\rho dz \right], \end{aligned} \quad (2.18)$$

together with

$$\phi = \psi(z)Q_0(\rho, z). \quad (2.19)$$

Note that there is no available gauge freedom to eliminate the off-diagonal, $d\rho dz$ -term in the metric (2.18), because the gauge is fixed by the choice of reference metric, which assigns a physical meaning to the ρ and z coordinates. In other words, in the context of the De Turck trick the condition $\xi^P = 0$ should be seen as fixing a coordinate gauge, and in this gauge the metric takes the form (2.18). Because of this, the metric (2.18) is not in FG form; we will return to this point below.

For each temperature, the functions $f(z)$, $g(z)$ and $\psi(z)$ in Eq. (2.18) are taken to be those of the homogeneous metastable solution approached as $\rho \rightarrow \infty$, which we chose as the reference metric. Hence, $Q_i(\rho, z)$ parametrize the deviation from this solution. Since this deviation must vanish far away from the bubble location, we impose the boundary conditions

$$\lim_{\rho \rightarrow \infty} Q_i(\rho, z) = 1 \quad \text{for } i = 0, \dots, 4, \quad \lim_{\rho \rightarrow \infty} Q_5(\rho, z) = 0. \quad (2.20)$$

In addition, we require regularity at $\rho = 0$.

Regarding the boundary conditions in the holographic direction, a near-boundary analysis shows that the different functions must approach the boundary as

$$\begin{aligned}
Q_1(\rho, z) &= 1 + q_{tt}(\rho)z^4 + O(z^6 \log z), \\
Q_2(\rho, z) &= 1 + q_{\rho\rho}(\rho)z^4 + O(z^6 \log z), \\
Q_3(\rho, z) &= 1 - \frac{1}{2} \left(4\Lambda^2 q_\phi(\rho) + q_{tt}(\rho) + q_{\rho\rho}(\rho) \right) z^4 + O(z^6 \log z), \\
Q_4(\rho, z) &= 1 + 2\Lambda^2 q_\phi(\rho)z^4 + O(z^6 \log z), \\
Q_5(\rho, z) &= q_{\rho z}(\rho)z^5 + \frac{\Lambda^2}{2z_H} q'_\phi(\rho)z^5 \log z + O(z^6 \log z), \\
Q_0(\rho, z) &= 1 + q_\phi(\rho)z^2 + O(z^4).
\end{aligned} \tag{2.21}$$

The appearance of logarithms in these formulas may be surprising given that there are no conformal anomalies in the boundary theory under consideration. The reason is that the metric (2.18) is not written in FG form, since $G_{\rho z} \neq 0$. This point will become clear below. We see that, in addition to the parameters of the chosen background solution, new undetermined functions of the radial coordinate appear in the expansion: $q_{tt}(\rho)$, $q_{\rho\rho}(\rho)$, $q_\phi(\rho)$ and $q_{\rho z}(\rho)$. These will account for the inhomogeneities of the different thermodynamic quantities, as we explain in the next Section.

Regularity at the horizon imposes the following boundary conditions:

$$Q_1(\rho, z_H) = Q_4(\rho, z_H), \quad \partial_z Q_5(\rho, z_H) - \frac{Q_5(\rho, z_H)}{2z_H} = 0, \quad \partial_z Q_i(\rho, z_H) = 0 \quad \text{for } i = 1, 2, 3. \tag{2.22}$$

The first condition ensures that the temperature is constant along the horizon despite its inhomogeneous nature.

If we evaluate the norm of ξ on the asymptotic expansion shown in Eq. (2.21), we obtain that $\xi_A \xi^A = 0$ implies the following relation between the coefficients:

$$q'_{\rho\rho}(\rho) = -\frac{1}{\rho} \left(4\Lambda^2 q_\phi(\rho) + q_{tt}(\rho) + 3q_{\rho\rho}(\rho) \right) - \frac{3}{2} \Lambda^2 q'_\phi(\rho). \tag{2.23}$$

In the next Section we will see that this equation is in fact equivalent to the conservation of the stress tensor in the boundary QFT.

Below we will describe in detail the solutions to the Einstein-dilaton equations with these boundary conditions. Each solution can be constructed from the previous one by slightly changing the temperature and letting the profiles of the different functions relax to a new solution, via a Newton-Raphson procedure. One of the most challenging steps in these types of problems is to get the first non-trivial solution. To construct it, we started with a homogeneous solution close to the turning point, namely to the lowest-temperature state on the metastable branch (see Fig. 2). At this point we expect the bubble amplitude to be small, i.e. we expect the bubble solution to be everywhere close to the homogeneous state. Then we seeded the Newton-Raphson algorithm with the homogeneous metastable solution plus a small convenient perturbation. After a few trials and errors the code converged to a new, inhomogeneous solution. Details of the computations can be found in Appendix A.

2.4 Thermodynamics

Once the numerical solutions for the critical bubbles are constructed, we can compute their thermodynamic properties. As usual, the entropy of each solution can be computed from the area of the horizon:

$$\begin{aligned} S &= \frac{2\pi}{\kappa_5^2} \text{Area}(z = z_{\text{H}}) \\ &= \frac{2L^3}{\kappa_5^2} \frac{\pi g_{\text{H}}^{3/2}}{z_{\text{H}}^3} \times 4\pi \int_0^\infty d\rho \rho^2 Q_2(\rho, z_{\text{H}})^{1/2} Q_3(\rho, z_{\text{H}}) \\ &\equiv 4\pi \int_0^\infty d\rho \rho^2 s(\rho), \end{aligned} \quad (2.24)$$

where the last identity defines what we mean by the entropy density per unit physical volume in the boundary theory—we will come back to this point at the end of this section. In Eq. (2.24), the term on the left of the “ \times ” is the entropy density of the metastable, homogeneous solution to which the bubble solution asymptotes as $\rho \rightarrow \infty$. In the homogeneous case $Q_2 = Q_3 = 1$ and the term on the right of the “ \times ” gives simply the volume of flat space, which is of course infinite. However, the difference between the entropy of the bubble solution, (2.24), and that of the corresponding homogeneous (metastable) one, S_+ , is given by

$$\Delta S = S - S_+ = \frac{2L^3}{\kappa_5^2} \frac{\pi g_{\text{H}}^{3/2}}{z_{\text{H}}^3} \times 4\pi \int_0^\infty d\rho \rho^2 \left(Q_2(\rho, z_{\text{H}})^{1/2} Q_3(\rho, z_{\text{H}}) - 1 \right), \quad (2.25)$$

and is finite. Following Ref. [81], we will use an analogous notation, $\Delta X = X - X_+$, for any quantity X .

To compute the temperature, we note that the horizon is generated by the Killing vector field

$$\zeta = \partial_t, \quad (2.26)$$

which is timelike for $z < z_{\text{H}}$ and null at $z = z_{\text{H}}$, i.e. $\zeta_M \zeta^M|_{z=z_{\text{H}}} = 0$. The surface gravity and the temperature are thus given by

$$\kappa_{\text{H}}^2 = -\frac{1}{2} (\nabla^M \zeta^N) (\nabla_M \zeta_N) \Big|_{z=z_{\text{H}}} = f_{\text{H}} \quad (2.27)$$

and

$$T = \frac{\kappa_{\text{H}}}{2\pi} = \frac{f_{\text{H}}^{1/2}}{2\pi}, \quad (2.28)$$

respectively. Recall that f_{H} has units of energy squared—see Eq. (2.10). Note that, as expected, the temperature is constant all along the horizon despite the inhomogeneous nature of the latter, and it coincides with the temperature of the metastable, homogeneous state to which the bubble solution asymptotes. Physically, this property is a consequence of the 0th law of black hole mechanics.

To obtain the remaining properties of the critical bubbles we use the well-known holographic renormalization procedure [82–85], whose details we discuss in Appendix B. To

implement this procedure, it is convenient to rewrite the metric in FG coordinates. In other words, we perform a change of variables $\tilde{z} = \tilde{z}(\rho, z)$, $\tilde{\rho} = \tilde{\rho}(\rho, z)$ such that the metric (2.18) in the tilde coordinates takes the form (2.9). Only the coordinate transformation near the boundary is needed, which takes the form

$$\begin{aligned}\tilde{z} &= z + \frac{1}{4} \Lambda q_\phi(\rho) z^5 + O(z^7 \log z), \\ \tilde{\rho} &= \rho + \frac{1}{36} \left(6z_{\text{H}} q_{\rho z}(\rho) - 2\Lambda^2 q'_\phi(\rho) + 3\Lambda^2 q'_\phi(\rho) \log z \right) z^6 + O(z^8 \log(z)).\end{aligned}\tag{2.29}$$

Note that ρ and $\tilde{\rho}$ coincide at the boundary, i.e. at $z = 0$. For this reason we can use them interchangeably in the UV quantities below that do not depend on \tilde{z} .² The near boundary expansion in terms of the FG coordinates becomes

$$\begin{aligned}g_{\mu\nu}(\tilde{z}, x) &= \frac{L^2}{\tilde{z}^2} \left(\eta_{\mu\nu} + \frac{\Lambda^2}{3} \eta_{\mu\nu} \tilde{z}^2 + \gamma_{(4)\mu\nu}(\rho) \tilde{z}^4 + O(\tilde{z}^6) \right), \\ \phi(\tilde{z}, x) &= \tilde{z} \left(\Lambda + \phi_{(2)}(\rho) \tilde{z}^2 + O(\tilde{z}^4) \right),\end{aligned}\tag{2.30}$$

where now $\gamma_{(4)\mu\nu}(\rho)$ and $\phi_{(2)}(\rho)$ are combinations of the undetermined UV parameters appearing in Eqs. (2.12) and (2.21). In contrast to Eq. (2.21) (see also Appendix B) there are no logarithms in the FG form of the metric or the scalar field, consistently with the fact that there are no conformal anomalies in the boundary theory. The logarithms appear in the change of variables (2.29) from the FG coordinates $\tilde{\rho}, \tilde{z}$ to those in Eq. (2.18).

Once the metric is expressed in FG coordinates, it is straightforward to obtain an expression for the expectation value of the energy-momentum tensor, which in our (spherical) coordinates reads

$$\langle (T^{\text{QFT}})^\mu_\nu \rangle = \text{diag} \left(-e(\rho), p_{||}(\rho), p_\perp(\rho), p_\perp(\rho) \right).\tag{2.31}$$

Here $e(\rho)$ is the energy density, and $p_{||}$ and p_\perp are the longitudinal and transverse pressures with respect to the ∂_ρ direction, respectively. The general formula is given in Eq. (B.7), but there is an enormous simplification in our case because the boundary metric is flat and the source of the scalar operator is constant. Under these circumstances

$$\langle T_{\mu\nu}^{\text{QFT}} \rangle = \frac{2L^3}{\kappa_5^2} \left(\gamma_{(4)\mu\nu}(\rho) + \eta_{\mu\nu} \left(\Lambda \phi_{(2)}(\rho) + \left(\lambda_4 - \frac{1}{18} \right) \Lambda^4 \right) \right).\tag{2.32}$$

From this we conclude that the total energy is

$$\begin{aligned}E &= 4\pi \int_0^\infty d\rho \rho^2 e(\rho) \\ &= \frac{2L^3}{\kappa_5^2} \times 4\pi \int_0^\infty d\rho \rho^2 \left(-f_4 + \frac{\Lambda^4}{18} - \lambda_4 \Lambda^4 - \Lambda v - \frac{3}{2} \Lambda^2 q_\phi(\rho) - q_{tt}(\rho) \right),\end{aligned}\tag{2.33}$$

²This would not apply to functions evaluated at the horizon.

while the pressures read

$$\begin{aligned} p_{\parallel} &= \frac{2L^3}{\kappa_5^2} \left(-\frac{f_4}{3} + \frac{\Lambda^4}{54} + \lambda_4 \Lambda^4 + \frac{\Lambda v}{3} + \frac{3}{2} \Lambda^2 q_\phi(\rho) + q_{\rho\rho}(\rho) \right), \\ p_{\perp} &= \frac{2L^3}{\kappa_5^2} \left(-\frac{f_4}{3} + \frac{\Lambda^4}{54} + \lambda_4 \Lambda^4 + \frac{\Lambda v}{3} + \frac{1}{2} \left(-\Lambda^2 q_\phi(\rho) - q_{tt}(\rho) - q_{\rho\rho}(\rho) \right) \right). \end{aligned} \quad (2.34)$$

Notice that, as for the entropy density, the corresponding homogeneous expressions are obtained by setting the inhomogeneity to zero, $q_{tt}(\rho) = q_{\rho\rho}(\rho) = q_\phi(\rho) = 0$, in which case $p_{\parallel} = p_{\perp} \equiv p$. The energy density and the pressure of the homogeneous solutions read

$$e = \frac{2L^3}{\kappa_5^2} \left(-f_4 + \frac{\Lambda^4}{18} - \lambda_4 \Lambda^4 - \Lambda v \right), \quad p = \frac{2L^3}{\kappa_5^2} \left(-\frac{f_4}{3} + \frac{\Lambda^4}{54} + \lambda_4 \Lambda^4 + \frac{\Lambda v}{3} \right), \quad (2.35)$$

respectively.

In analogy with the entropy, we consider the energy difference between the inhomogeneous and the homogeneous solutions. This takes the form

$$\Delta E \equiv E - E_+ = \frac{2\pi L^3}{\kappa_5^2} \times 4\pi \int_0^\infty d\rho \rho^2 \left(\frac{5}{2} \Lambda^2 q_\phi(\rho) + 3q_{\rho\rho}(\rho) + \rho q'_{\rho\rho}(\rho) \right) < 0, \quad (2.36)$$

and is finite. The negative sign of ΔE is due to the fact that the bubble replaces a volume of high-energy phase by one of low-energy phase. With all this information we can also find the free energy as

$$F = E - TS. \quad (2.37)$$

The free energy difference between the critical bubble and the homogeneous metastable state is therefore

$$\Delta F \equiv F - F_+ = \Delta E - T\Delta S. \quad (2.38)$$

This will play a crucial role below, since it determines the nucleation rate of the critical bubbles. In Appendix C we show that F/T coincides with the on-shell Euclidean action, as expected.

Holographic renormalization also provides an expression for the expectation value of the scalar operator in terms of the asymptotic data, Eq. (B.9), which in our case becomes

$$\langle \mathcal{O} \rangle = \frac{2L^3}{\kappa_5^2} \left(-2\phi_{(2)}(\rho) - 4\lambda_4 \Lambda^3 \right) = \frac{2L^3}{\kappa_5^2} \left(-2q_\phi(\rho) - 2v - 4\lambda_4 \Lambda^3 \right). \quad (2.39)$$

Note the appearance of Newton's constant in front of all the quantities above. To translate it to a gauge theory quantity, we will use the coefficient of the Euler density appearing in the Weyl anomaly of the dual field theory (see Ref. [82]),

$$a = \frac{4L^3}{\kappa_5^2} \propto N^2. \quad (2.40)$$

Here we have indicated explicitly the fact that, in top-down scenarios, this quantity is proportional to the number of degrees of freedom in the dual QFT.

We close this section with an observation regarding the densities of thermodynamic quantities for inhomogeneous solutions. The energy density and the pressure are always unambiguously defined at any spacetime point because they can be extracted from the stress tensor. The temperature is also well defined because the 0th law of black hole mechanics implies that it is constant along the horizon. In contrast, defining the entropy density requires the choice of a map between points at the boundary and points at the horizon, and this is not unique. In Eq. (2.24) we chose the map suggested by the gauge in which the metric takes the form (2.18). From the entropy and the energy densities we then define the free energy density through the usual relation

$$f = e - Ts. \quad (2.41)$$

Needless to say, the free energy density suffers from the same ambiguities as the entropy density. To illustrate this, we note that we would arrive at a different definition if we used the tilde coordinates in Eq. (2.29) in which the metric takes the FG form. A third natural choice would be to map the points at the boundary to points at the horizon by shooting in-going null geodesics from the boundary, as suggested by the fluid/gravity correspondence [86]. Crucially, the physical results are independent of these choices, since they depend only on integrated quantities (such as the nucleation rate) or can be expressed in terms of well-defined observables, such as the energy density (for instance, the bubble wall profile).

3 Results

3.1 Phase diagram

Let us now show our results. For concreteness, we will restrict our analysis to the case $\lambda_4 = -1/4$ and $\lambda_6 = 1/10$. We expect qualitatively similar results for other values for which the theory also exhibits a FOPT. Once these parameters are specified, we can obtain a family of homogeneous black brane solutions parametrized by the value of the scalar ϕ at the horizon, ϕ_H . Some homogeneous solutions, with different values of ϕ_H , share the same value of the temperature in units of the source, T/Λ . This leads to the mutivaluedness visible in Fig. 2, which is characteristic of a FOPT. In the mutivalued region, the thermodynamically preferred phase (in the canonical ensemble) is that with the lowest free energy. In Fig. 3 (top), where we show the free energy density as a function of the temperature, we see that the system undergoes a FOPT at the critical temperature $T = T_c \simeq 0.3959\Lambda$, where the curve crosses itself. Since for homogeneous solutions the free energy equals minus the pressure, it is clear that the latter is continuous across the FOPT, while the energy density jumps by almost a factor of 3. This also implies that below $T = T_c$ the stable phase has a higher pressure than the metastable phase, even though it has a lower energy density—see Fig. 3 (bottom).

Below T_c there is a range of temperatures $T \in (T_0, T_c)$, with $T_0 \simeq 0.3879\Lambda$, where a *supercooled* metastable branch of states exists. We will find it useful to define the *relative temperature difference* as

$$\mathcal{T}(T) = \frac{T - T_0}{T_c - T_0}. \quad (3.1)$$

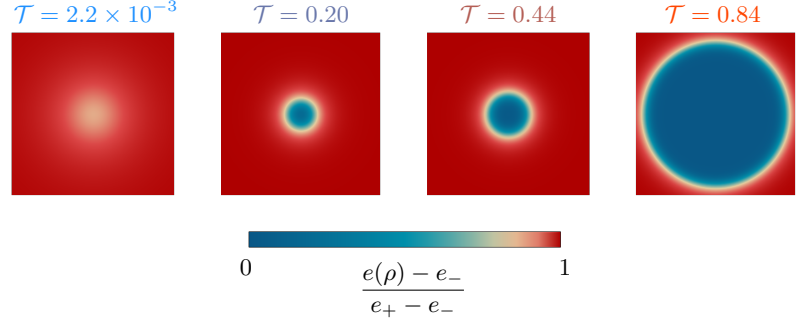


Figure 2: Energy density as a function of temperature for the theory with $\lambda_4 = -1/4$, $\lambda_6 = 1/10$. The thick solid curves correspond to the two branches of stable configurations. The two vertical, thin, dashed black lines indicate the location of the turning point at $T = T_0$, where the spinodal branch begins, and the first-order phase transition at $T = T_c$. The two dashed curves that extend between the critical temperature and the corresponding turning point are metastable branches. They are connected by the spinodal branch (intermediate dotted curve), where the system is both thermodynamically and dynamically unstable. The gray solid curve that interpolates between T_0 and T_c indicates the energy density at the center of the critical bubbles. At the top, we present the density plot for the relative energy density of four representative bubble solutions, indicating the value of their relative temperature difference \mathcal{T} , defined in Eq. (3.1). Their energy profiles expand from the metastable branch (dots) to the corresponding value at the center of the bubble (squares), as indicated by the arrows. In the legend, e_+ and e_- refer to the energy densities in the metastable, high-energy phase and in the stable, low-energy phase, respectively.

This quantity takes values between zero (at T_0) and one (at T_c), and hence it is helpful to indicate the position of each solution in the metastable branch. Note that T_0 is very close

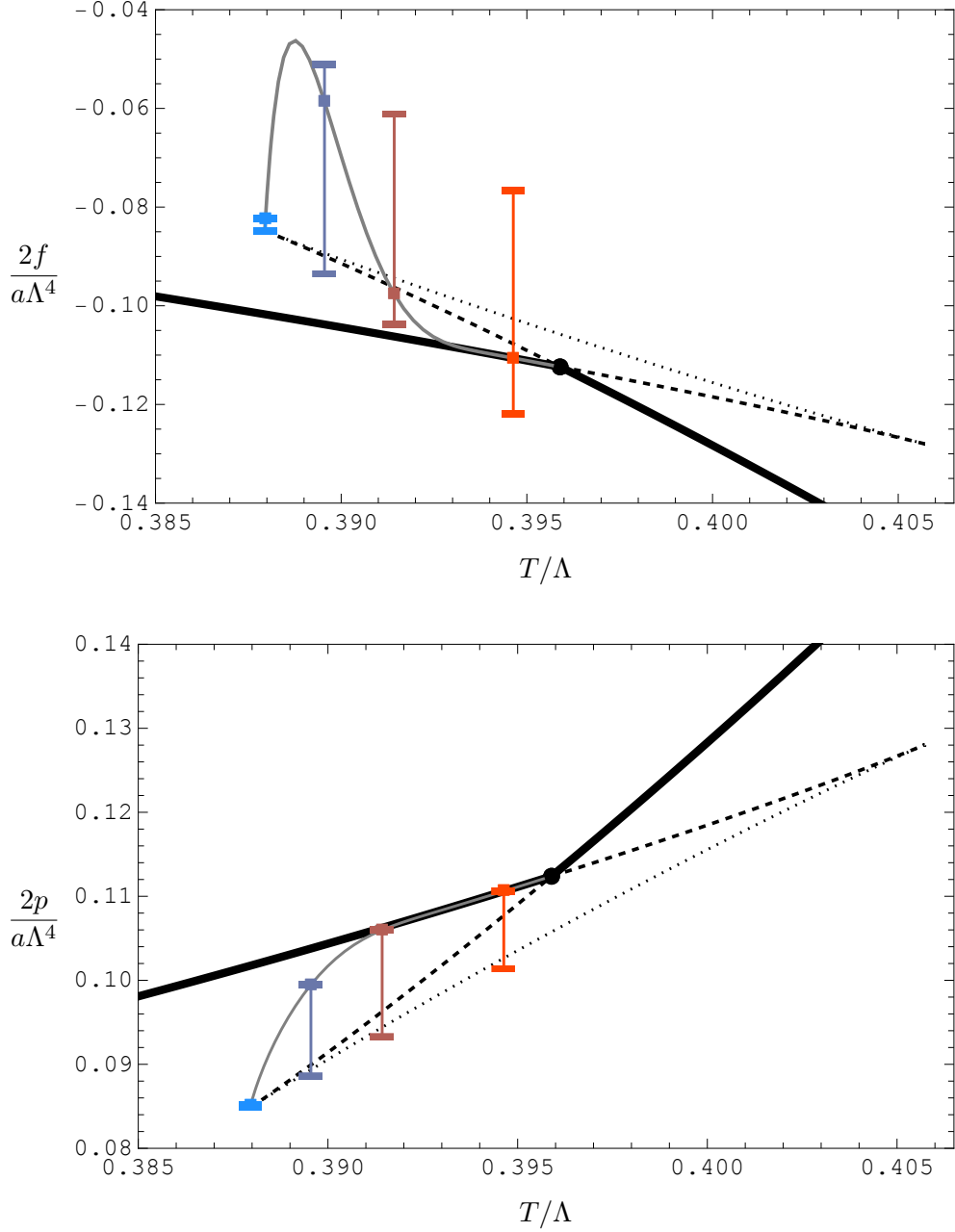


Figure 3: Free energy density defined through (2.41) (top) and pressure (bottom) of the homogeneous solutions as functions of the temperature. The conventions are the same as in Fig. 2, with the thickest curves representing homogeneous, stable states. The critical temperature, marked by a thick black dot, is the point where these curves cross each other. For the same four bubbles shown in Fig. 2, we have drawn bars indicating the range probed by each bubble (see also Fig. 4), extending from the origin (marked by a square) to infinity (on the metastable dashed branch). Close to T_c , the state at the bubble center lies near the stable homogeneous state, although the bubble wall itself remains non-trivial. Note that $p = -f$ for homogeneous states but not for inhomogeneous ones, as expected on general grounds.

to T_c , since

$$\frac{T_c - T_0}{T_c} \simeq 2.01 \times 10^{-2}. \quad (3.2)$$

Similarly, a *superheated* metastable branch exists above T_c . The homogeneous states on these branches have higher free energy than those in the preferred phases but they are dynamically stable against small perturbations. Whether a perturbation triggers the phase transition depends on its size, as will be clear from our analysis of critical bubbles.

3.2 Critical bubbles

Let us discuss the solutions and properties of the critical bubbles, focusing on the metastable supercooled branch. As we anticipated, each of the critical bubbles we construct asymptotes to one of the states on this metastable branch. To construct the first one, we chose a homogeneous state close to the turning point at $T = T_0$ and seeded a Newton-Raphson algorithm with this homogeneous metastable solution plus a small perturbation. After few trials and errors the code converged to a new, inhomogeneous solution. Once the first bubble is constructed, we vary slightly the value of T/Λ and use the first solution to construct the second one. Then we iterate this process until we cover the full range of temperatures $T \in (T_0, T_c)$. Details of the computations can be found in Appendix A.

As we vary the temperature and find different solutions, we uncover two qualitatively distinct regimes depending on whether or not T is close to T_c , as shown in Fig. 4. If T is close to T_c , then the bubbles consist of three parts: the interior of the bubble, where the system is approximately in the low-energy, stable phase; the exterior, which lies in the high-energy, metastable phase; and a wall that separates these two regions. In particular, the profile of several quantities such as the energy density or the expectation value of the scalar operator become well approximated by a hyperbolic tangent of the form

$$e(\rho) \simeq e_0 + e_m \tanh\left(\frac{\rho - R}{\ell}\right), \quad (3.3)$$

as illustrated in Fig. 5. The bubbles in this regime have a characteristic radius R and thickness ℓ . In order to understand how these quantities depend on the temperature, we fit the profile of the bubbles to Eq. (3.3). An alternative definition of the size of the bubble can be the value of $\rho = R$ where the profile for the energy density acquires its mean value between the energy density at infinity and at the center of the bubble, i.e., by the equation

$$e(\rho = R) = \frac{1}{2} (e(0) + e(\infty)) = \frac{1}{2} (e(0) + e_+). \quad (3.4)$$

We show these two alternative definitions of R in Fig. 6, where we see that they essentially coincide.

As the temperature decreases, the bubble shrinks, and its interior eventually no longer reaches the low-energy (stable) phase. This behavior is illustrated in Fig. 2, where the energy density at the center of the bubble is shown as a gray curve overlaid on the phase diagram. At some point, the profile of the bubble ceases to be well approximated by two homogeneous phases separated by a wall. Indeed, close to T_0 we reach a second,

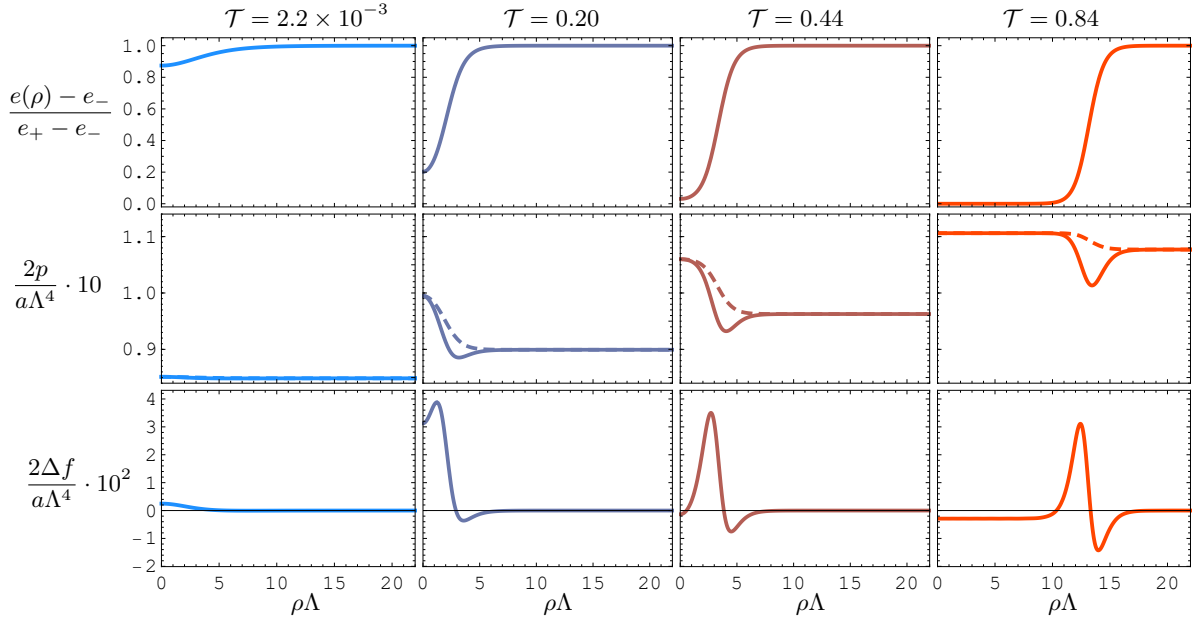


Figure 4: (Top) Energy density of a bubble as a function of the radial direction, normalized to the difference between the metastable (+) and stable (−) branches, for the four different choices of \mathcal{T} indicated on each column, where \mathcal{T} is defined in Eq. (3.1). Near T_0 (left, $\mathcal{T} = 0$) the profile of the energy density is Gaussian and its characteristic size grows as T_0 is approached. On the other side, near T_c (right, $\mathcal{T} = 1$), the profile becomes closer and closer to a hyperbolic tangent. The profiles of the entropy density and the expectation value of \mathcal{O} exhibit qualitatively similar behavior. (Middle) Transverse (solid curves) and longitudinal (dashed curves) pressures as a function of the radial direction for the same values of the temperature. These coincide at the origin, where isotropicity is restored, and at infinity, where the asymptotic, metastable, homogeneous state is recovered. (Bottom) Free energy density difference, $\Delta f = f(\rho) - f_+$, as a function of the radial direction for the same values of the temperature. These are the profiles that we integrate to obtain the bubble action.

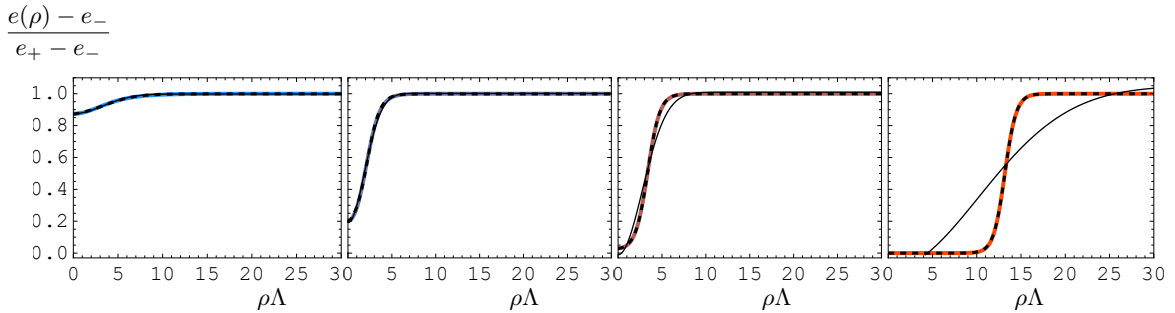


Figure 5: Best Gaussian (thin, solid) and hyperbolic tangent (dashed, thick) fits on top of the energy density profile from Fig. 4 (top). The hyperbolic tangent appears to approximate the profiles well in all the range of temperatures, but it fails to give the correct Newman boundary condition at $\rho = 0$, specially close to T_0 . The Gaussian profile Eq. (3.5), in contrast, has a minimum at the origin, but fails to reproduce the profile away from T_0 .

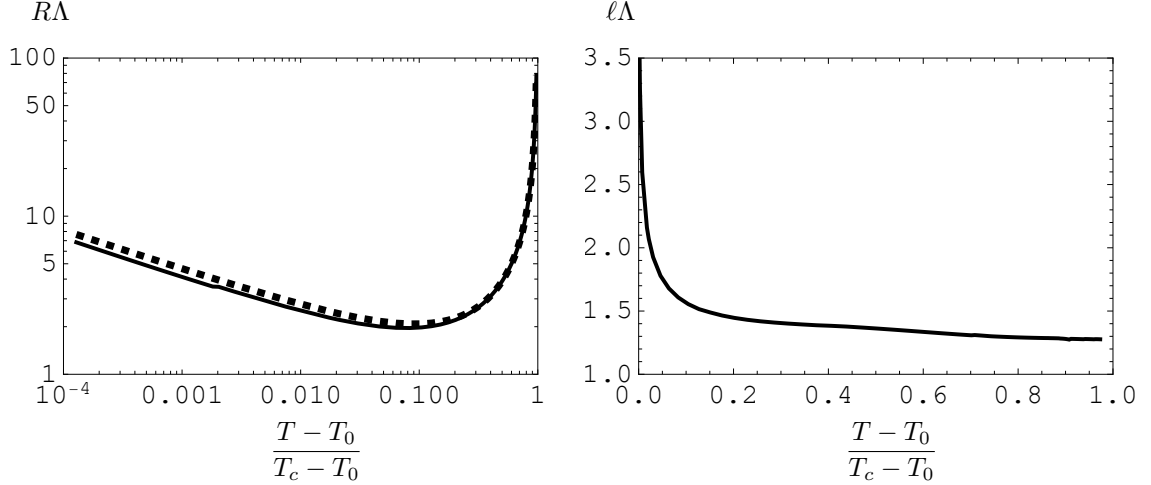


Figure 6: (Left) Radius of the bubbles from Eq. (3.3) (solid) and Eq. (3.4) (dashed) as a function of the temperature. (Right) Width of the bubble wall from Eq. (3.3) as a function of the temperature.

qualitatively different regime where the profile of different quantities becomes Gaussian, for instance

$$e(\rho) \simeq e_0 + e_p \exp\left(-\frac{\rho^2}{2b^2}\right). \quad (3.5)$$

Here we see that as the temperature decreases towards T_0 the bubbles grow again and become flatter in the sense that the difference between the energy density at the origin and infinity decreases.

It is worth discussing the pressure profiles for these solutions. As we mentioned, despite the fact that the solutions are static and obey $\nabla_\mu T^{\mu\nu} = 0$, the pressures need not be the same in all directions, since the solutions are anisotropic. In fact, the conservation of the stress tensor reduces to only one non-trivial equation:

$$0 = \nabla_\mu T^{\mu\rho} = p'_{||}(\rho) + \frac{2}{\rho} (p_{||}(\rho) - p_\perp(\rho)). \quad (3.6)$$

As usual, from the bulk perspective this equation is one of the constraints in the Einstein equations evaluated near the boundary. The difference between the longitudinal and transverse pressures is illustrated in Fig. 4. In particular, we see that the longitudinal pressure is monotonic, whereas the transverse one is not. Nevertheless, they coincide both at the origin and at infinity, where rotational symmetry requires isotropy.

Interestingly, if we substitute the expression for the pressures (2.34) into Eq. (3.6), we find precisely Eq. (2.23), which is satisfied on-shell (when $\xi^A = 0$). A way to phrase this result is that DeTurck solitons in this system (i.e. solutions with $\xi^A \neq 0$), if they existed, would fail to satisfy energy-momentum conservation in the boundary theory. In addition, Eq. (3.6) provides a check of our numerics: we can calculate p_\perp and $p_{||}$ from the numerical solutions and verify that they indeed satisfy Eq. (3.6).

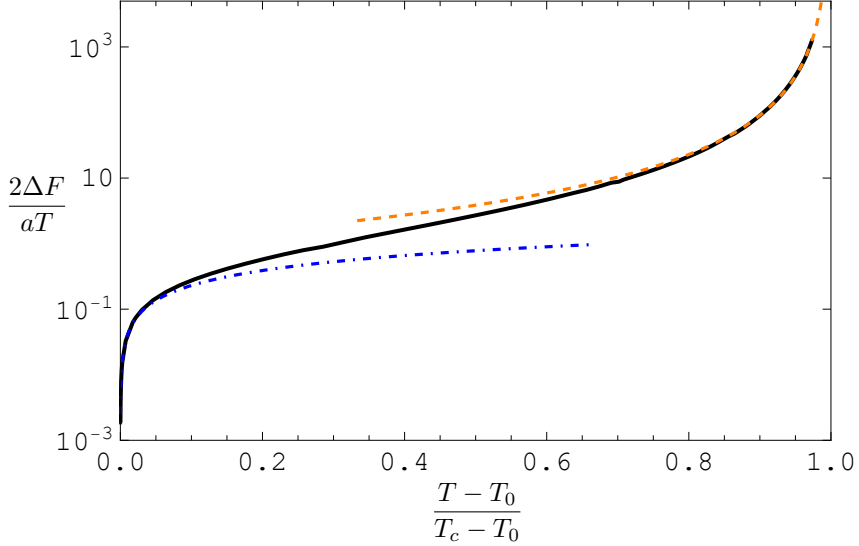


Figure 7: Bubble action controlling the nucleation probability. The solid black curve corresponds to the microscopic result provided by holography. The blue, dot-dashed curve corresponds to the numerical fit in Eq. (3.13), which is compatible with $\Delta F \propto (T - T_0)^{3/4}$. The dashed orange curve represents the thin-wall approximation, Eq. (3.10), with a string tension given by Eq. (3.12).

3.3 Nucleation rate

A homogeneous, metastable state decays to the stable, thermodynamically preferred state via the nucleation of critical bubbles. In the semiclassical approximation, the probability to nucleate a bubble per unit volume and unit time -the nucleation rate- is given by (see e.g. [81])

$$\mathcal{P}(T) = a_0 e^{-\beta \Delta F}, \quad (3.7)$$

where $\beta = 1/T$ and the prefactor a_0 is usually of order $a_0 \sim T^4$. We see that the probability is exponentially sensitive to the free energy difference. We will refer to the product $\beta \Delta F$ as “the bubble action”. This quantity is given by Eq. (2.38) and is plotted in Fig. 7. Let us now analyze the two limiting regimes, $T \rightarrow T_c$ and $T \rightarrow T_0$, which are clearly visible in the figure.

Close to the critical temperature $\ell \ll R$ and the *thin wall approximation* applies [81]. As mentioned in Sec. 3.2, in this regime the profile of a bubble is well approximated by a hyperbolic tangent—see Eq. (3.3)—and ΔF decomposes into two contributions: one from the pressure difference (times the volume of the bubble) and a second one from the wall itself, proportional to the area of the bubble:

$$\Delta F \simeq -\frac{4\pi R^3}{3} \Delta p + 4\pi R^2 \sigma. \quad (3.8)$$

Here, $\Delta p = p_- - p_+ > 0$ is the pressure difference between the low-energy stable and the high-energy metastable homogeneous phases, R is the radius of the bubble, and σ is the *surface tension*. This expression is motivated by the observation that the thickness of the bubble saturates as T_c is approached—see Fig. 6. Extremizing Eq. (3.8) we obtain an

expression for the radius of the critical bubble in this regime:

$$R \simeq \frac{2\sigma}{\Delta p}. \quad (3.9)$$

Note that both σ and Δp scale as $a \sim N^2$, so R is N -independent. Substituting (3.9) into (3.8) we find

$$\Delta F \simeq \frac{16\pi}{3} \frac{\sigma^3}{(\Delta p)^2}. \quad (3.10)$$

The pressure difference vanishes at $T = T_c$, so near T_c we have

$$\Delta p \propto (T - T_c) \quad \Rightarrow \quad \Delta F \propto (T - T_c)^{-2}. \quad (3.11)$$

This is confirmed by Fig. 7, where this behavior is indicated by the fitted dashed orange curve.

From the fit in the figure we also obtain the surface tension

$$\sigma \simeq 9.64 \times 10^{-3} a\Lambda^3 \simeq 1.55 \times 10^{-1} aT_c^3. \quad (3.12)$$

As expected from large- N counting arguments, this quantity scales as $a \propto N^2$. However, its value is numerically suppressed relative to the naive dimensional estimates $\sigma \sim a\Lambda^3$ and $\sigma \sim aT_c^3$, respectively. Note that even a mild suppression in σ can lead to a significant suppression of the bubble action. Interestingly, lattice studies [87, 88] have found analogous behavior in the deconfinement transition of large- N $SU(N)$ YM theories, leading to significantly less supercooling than expected from the naïve scaling [89]. We will show that the same phenomenon arises in our setup and that, within the effective description of the bubbles, it can be traced back to a suppression of the kinetic term.

In the opposite limit, close to T_0 , we find

$$\Delta F \propto (T - T_0)^x, \quad (3.13)$$

with $x \simeq 0.76$. This result is obtained from a power-law fit to the ten data points closest to T_0 , which span one order of magnitude:

$$1.2 \times 10^{-4} \leq \frac{T - T_0}{T_c - T_0} \leq 1.3 \times 10^{-3}. \quad (3.14)$$

We believe that our result is compatible with $x = 3/4$ within our numerical precision. Interestingly, this is different from the exponent $x = 3/2$ found in Ref. [3]. We will come back to this point below.

4 Effective description

The holographic results above provide a fully microscopic description of the critical bubbles. In this section we will use them to verify what features are well captured by a local, two-derivative effective action, which is frequently used in the literature. This effective action takes the form

$$S_{\text{eff}}(T) = \int_0^\beta d\tau \int d^3x \left(\frac{1}{2} Z(\varphi, T) (\nabla \varphi)^2 + V_{\text{eff}}(\varphi, T) \right), \quad (4.1)$$

where φ is some order parameter that jumps discontinuously across the phase transition. Note that we are omitting a $(\partial_\tau \varphi)^2$ term, since we are only considering $O(3)$ -symmetric configurations. The choice of order parameter is not unique, and a natural choice for φ is the VEV of the scalar operator dual to the bulk ϕ , namely

$$\varphi = \langle \mathcal{O} \rangle. \quad (4.2)$$

Note that this field has dimensions of (energy)³, and consequently $Z(\varphi, T)$ has dimensions of (energy)⁻⁴. In addition, since the effective action and φ scale as N^2 , it follows that $Z \sim N^{-2}$.

The $O(3)$ -symmetric critical bubbles are classical solutions of the equations of motion that follow from S_{eff} . In the spherically symmetric case they reduce to one equation in terms of the radial coordinate ρ :

$$\frac{d^2\varphi}{d\rho^2} + \frac{2}{\rho} \frac{d\varphi}{d\rho} + \frac{1}{2} \frac{\partial_\varphi Z(\varphi, T)}{Z(\varphi, T)} \left(\frac{d\varphi}{d\rho} \right)^2 - \frac{\partial_\varphi V_{\text{eff}}(\varphi, T)}{Z(\varphi, T)} = 0, \quad (4.3)$$

subject to the boundary conditions $\varphi'(0) = 0$ and $\varphi(\infty) = \varphi_+$, with φ_+ the value of the order parameter in the metastable state with temperature T .

The effective action is completely determined by the microscopic theory, in which it can be computed via a Legendre transform of the generating functional. We will review this procedure in Section 4.1, and in Section 4.2 we will use it to compute the effective action in our holographic model following Ref. [71]. We will then find the critical bubbles in this effective description and compare them to those in the microscopic description. In phenomenological analysis some simplifying assumptions about the functional form of Z and V_{eff} are often made. In Section 4.3 we will assess the validity of these approximations in our case.

4.1 Definition of the effective action

Here we will review how to construct the effective action following the presentation in Ref. [71]. We will see that this can be constructed from the quantum effective action evaluated on homogeneous equilibrium states.

The quantum effective action $\Gamma[\varphi]$, also known as the one-particle-irreducible (1PI) effective action, is defined as the Legendre transform of the Euclidean generating functional

$$W[J] = -\log Z[J], \quad (4.4)$$

where $Z[J]$ denotes the path integral in the presence of an external source $J(x)$. Explicitly, the effective action is given by

$$\Gamma[\varphi] \equiv W[J] - \int d^4x J(x) \varphi(x), \quad (4.5)$$

with the Euclidean spacetime integral defined as

$$\int d^4x \equiv \int_0^\beta d\tau \int d^3x \equiv \beta V_3.$$

In this expression, $\varphi(x)$ is the expectation value of the operator sourced by $J(x)$, given by the variation of the generating potential with respect to the source,

$$\frac{\delta W[J]}{\delta J(x)} = \varphi(x). \quad (4.6)$$

Similarly, by construction, the source can be obtained as the variation of the effective action with respect to φ :

$$\frac{\delta \Gamma[\varphi]}{\delta \varphi(x)} = -J(x). \quad (4.7)$$

This equation has an important consequence, as it implies that any sourceless state of the theory can be obtained by solving the classical equations of motion derived from the effective action. Unfortunately, finding $\Gamma[\varphi]$ exactly is in general not possible, but progress can still be made with some simplifying assumptions.

Let us first assume that, in the absence of sources, the partition function is dominated by a saddle point with a given value of the expectation value $\varphi(x) = \varphi_0(x)$. Then, the generating functional can be expanded in the source as

$$W[J] = W_0 + \int d^4x J(x) \varphi_0(x) + \frac{1}{2} \int d^4x d^4y G_0(x, y) J(x) J(y) + \dots, \quad (4.8)$$

with G_0 the connected correlator of the operator evaluated at the saddle point. The expectation value in the presence of a non-zero source becomes

$$\varphi(x) = \frac{\delta W[J]}{\delta J(x)} = \varphi_0(x) + \int d^4y G_0(x, y) J(y) + \dots. \quad (4.9)$$

From this last expression we can solve for the source in terms of the expectation value using the inverse correlator

$$J(x) = \int d^4y G_0^{-1}(x, y) [\varphi(y) - \varphi_0(y)] + \dots. \quad (4.10)$$

Together with Eq. (4.8), this can be used in (4.5) to get an expression for the effective action to leading order:

$$\Gamma[\varphi] = W_0 - \frac{1}{2} \int d^4x d^4y G_0^{-1}(x, y) [\varphi(x) - \varphi_0(x)] [\varphi(y) - \varphi_0(y)] + \dots. \quad (4.11)$$

We emphasize that this expression is an expansion about the saddle $\varphi_0(x)$ and no gradient expansion has been made at this stage. Neglecting the higher order terms represented by “ \dots ”, the equations of motion derived from Eq. (4.11) are

$$\frac{\delta \Gamma[\varphi]}{\delta \varphi(x)} = - \int d^4y G_0^{-1}(x, y) [\varphi(y) - \varphi_0(y)] = 0. \quad (4.12)$$

By construction, the solutions correspond to configurations with zero source (see Eq. (4.7)), which can be expressed as

$$\varphi(x) = \varphi_0(x) + \eta(x), \quad (4.13)$$

where $\eta(x)$ belongs to the kernel of the inverse propagator.

We will now apply this general discussion to the construction of the effective action $S_{\text{eff}}(T)$ in Eq. (4.1). For this purpose, we begin by choosing a homogeneous equilibrium state φ_0 as the state around which we expand, i.e., we set $\varphi_0(x) = \varphi_0$, with $\partial_\mu \varphi_0 = 0$. Since the quantum effective action coincides with the free energy, for a homogeneous state we find that

$$\Gamma[\varphi_0] = W_0[\varphi_0] = \beta F_0 = \beta V_3 V_{\text{eff}}(\varphi_0, T). \quad (4.14)$$

Moreover, the requirement that φ_0 be an extremum of the effective action reduces, for a homogeneous configuration, to the condition that it extremizes the effective potential, $\partial_\varphi V_{\text{eff}}(\varphi_0, T) = 0$.

To get an expression for the kinetic term we need to consider inhomogeneous states. Let us linearize the effective action $S_{\text{eff}}(T)$ from Eq. (4.1) around the equilibrium state φ_0 , in the way suggested by Eq. (4.13). In Fourier space, indicated by quantities with tildes, the linearized equations of motion read

$$[Z(\varphi_0, T)q^2 + \partial_\varphi^2 V_{\text{eff}}(\varphi_0, T)] \tilde{\eta}(\omega = 0, q) = 0. \quad (4.15)$$

We impose that the solutions to these equations coincide with the solutions obtained from the quantum effective action, Eq. (4.12). It follows that the Fourier transform of the inverse correlator, \tilde{G}_0^{-1} , has a zero at values of the spatial momentum modulus $q^2 = P_0$ for which Eq. (4.12) vanishes. Close to these values

$$-\tilde{G}_0^{-1}(\omega = 0, q^2 \rightarrow P_0) \sim Z(\varphi_0, T)q^2 + \partial_\varphi^2 V_{\text{eff}}(\varphi_0, T) \rightarrow 0. \quad (4.16)$$

We have fixed a possible relative factor by demanding $\Gamma[\varphi] = S_{\text{eff}}(T)$ at quadratic order. The same value of q^2 corresponds to a pole of the correlator \tilde{G}_0 . Sufficiently close to this point

$$\tilde{G}_0(\omega = 0, q^2 \rightarrow P_0) \sim \frac{R_0}{q^2 - P_0}. \quad (4.17)$$

Inverting this expression, we see that the location of the pole, P_0 , and the value of the residue, R_0 , are related to the potential and kinetic terms of the effective action through

$$P_0 = -\frac{\partial_\varphi^2 V_{\text{eff}}(\varphi_0, T)}{Z(\varphi_0, T)}, \quad R_0 = -\frac{1}{Z(\varphi_0, T)}. \quad (4.18)$$

If the location and the residue of the pole are known, these relations can be used to extract the coefficient of the kinetic term, $Z(\varphi_0, T)$.

Note that, in general, the correlator of a composite operator, such as the one appearing in the holographic model under consideration, does not exhibit a single isolated pole, but rather a nontrivial analytic structure involving multiple poles and branch-cut singularities. Nevertheless, there is always a distinguished pole whose location in momentum space is controlled by the second derivative of the effective potential. This pole becomes parametrically separated from the others at the spinodal points, where two extrema coalesce and $\partial_\varphi^2 V_{\text{eff}}(\varphi_0, T)$ vanishes. In what follows, we assume that this pole provides the dominant contribution relevant for describing bubble configurations, while the effects of additional poles and branch cuts are parametrically suppressed and can be neglected. The results that we will obtain are consistent with this assumption.

4.2 Holographic construction of the effective action

In this section we will use holography to derive the effective action for the order parameter from first principles. We will then compare the results from this effective description to the microscopic ones.

To connect the previous discussion to our holographic model, let us consider a fixed temperature T and a fixed coupling Λ . This selects gravity solutions with a fixed value of the ratio Λ/T as the duals of saddle points of the QFT for which the source vanishes, $J(x) = 0$. The free energy of these saddle points can be found by drawing a vertical line in Fig. 3 at the corresponding value of Λ/T . Changing the temperature modifies the value of Λ/T that defines the sourceless saddle points, causing the vertical line to shift horizontally in the figure. Once these reference points are identified, we can consider solutions with a non-zero constant source $J(x) = J$, which will be those for which the leading order coefficient of the scalar field, see Eq. (2.12), is the sum of the coupling and the source, $\phi_s = \Lambda + J$.

From the gravity dual, Eq. (2.39) gives the expectation value of the dual operator as a function of ϕ_s , which, for a homogeneous configuration, reduces to

$$\varphi = \langle \mathcal{O} \rangle = \frac{2L^3}{\kappa_5^2} \left(-2v(\phi_s) - 4\lambda_4 \phi_s^3 \right). \quad (4.19)$$

For fixed values of Λ and T , this expression determines the expectation value of the operator as a function of the source: $\varphi = \varphi(J)$. The same function can be obtained from the derivative of the free energy density with respect to the source at fixed Λ and T (cf. Eq. (4.6)):

$$\varphi(J) = \left. \frac{\partial f}{\partial J} \right|_{T,\Lambda}. \quad (4.20)$$

For each choice of Λ/T we obtain a different curve for φ as a function of J , as shown in Fig. 8(left).³ We can invert this relation in the region where it is injective to obtain the source as a function of the expectation value, $J = J(\varphi)$, and the effective potential is obtained by integrating this function at fixed Λ and T (see Eq. (4.7)):

$$V_{\text{eff}}(\varphi, T) = \Gamma[\varphi] = f(\Lambda/T) - \int_{\varphi_0}^{\varphi} d\varphi' J(\varphi'), \quad \varphi_0 = \varphi(J=0). \quad (4.21)$$

The result is shown in Fig. 8(right) in terms of the difference between the potential and its value in the metastable state,

$$\Delta V_{\text{eff}}(\varphi, T) = V_{\text{eff}}(\varphi, T) - V_{\text{eff}}(\varphi_+, T). \quad (4.22)$$

In the figure we see the existence of two minima and one maximum in the region of the phase transition, as expected.⁴

³It is insightful to note that the curves in Fig. 8 (left) are shifted horizontally. This is because the source J (here constant) appears in the action exactly the same way as the coupling Λ ; since different curves correspond to different Λ (at fixed T) it is natural that the curves are shifted in J .

⁴A similar result for the same model was obtained in [90].

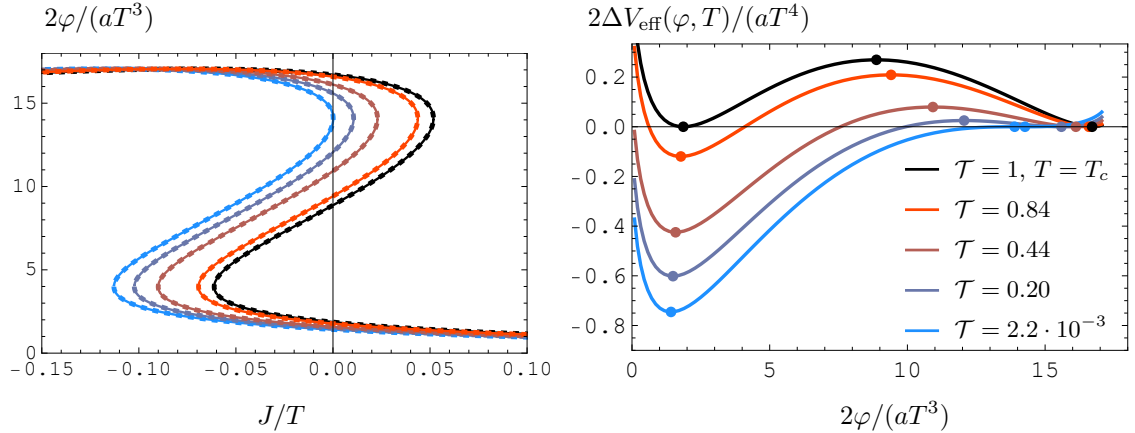


Figure 8: (Left) Order parameter φ as a function of the source J . Solid and dashed curves correspond to Eqs. (4.19) and (4.20), respectively. (Right) Effective potential obtained from the Legendre transform. The chosen values of the relative temperature difference \mathcal{T} , defined in Eq. (3.1), are shown in the legend.

With the effective potential in hand, we now turn to the determination of the kinetic-term coefficient $Z(\varphi, T)$. In doing so, we encounter a subtle issue related to scheme dependence. This subtlety arises if one follows the procedure of Refs. [71, 72], but was absent in those works because the scaling dimension of the scalar operator considered there forbids the introduction of finite counterterms.

The strategy adopted in those references was to compute the two-point function \tilde{G}_0 at zero frequency to quadratic order in an expansion in q^2/T^2 , then take the inverse to obtain \tilde{G}_0^{-1} to the same order, and finally identify $Z(\varphi, T)$ by comparing the result with Eq. (4.16). Following this procedure, the result for the inverse correlator in our case would be (see Appendix D)

$$\tilde{G}_0^{-1}(\omega = 0, q) = A_0 + B_0(\alpha)q^2 + O(q^4), \quad (4.23)$$

where the precise expressions for the coefficients A_0 and $B_0(\alpha)$ are given in Eq. (D.10). Here, α is an arbitrary coefficient of a local counterterm (B.5). The freedom to choose α is the freedom to choose a renormalization scheme, a point to which we will return shortly. Inverting Eq. (4.23) and comparing the result to Eq. (4.16) seemingly suggests that we should identify

$$\partial_\varphi^2 V_{\text{eff}}(\varphi, T) = -A_0, \quad Z_\alpha(\varphi, T) = -B_0(\alpha). \quad (4.24)$$

The first term correctly reproduces the second derivative of the effective potential obtained from Eq. (4.21), as illustrated in Fig. 9 (left). Note that, although the effective potential depends non-trivially on the choice of Λ/T , its second derivative $\partial_\varphi^2 V_{\text{eff}}(\varphi, T)$ does not, as illustrated by the figure.

The second term in Eq. (4.24) determines the coefficient of the kinetic term in the effective action; the full expression for Z_α is given in Eq. (D.12). The fact that it depends on the arbitrary coefficient α , as illustrated in Fig. 9 (right), would seemingly render the kinetic term scheme-dependent and hence physically ambiguous. However, this puzzle

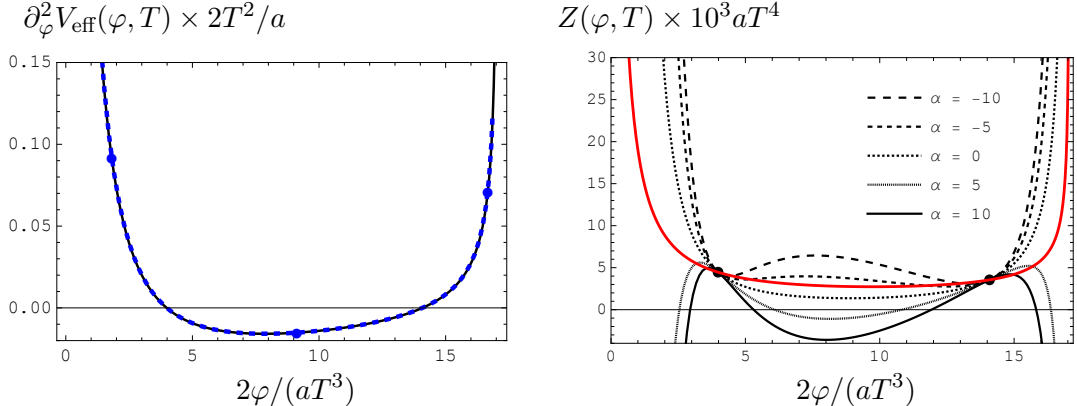


Figure 9: (Left) Second derivative of the effective potential as a function of φ , obtained from Eq. (D.11) and the first equation in (4.24) (solid black), and from taking the second derivative of the potential reconstructed by integrating the source in Eq. (4.21) (dashed blue). For illustration, the blue dots correspond to the equilibrium configurations at $T \simeq 0.3953\Lambda$, corresponding to $\mathcal{T} \simeq 0.93$, where \mathcal{T} is defined in Eq. (3.1). (Right) The correct coefficient of the kinetic term, obtained in Eq. (D.13) from the exact residue at the pole of the propagator, is shown in solid red. The black curves correspond to the scheme-dependent results that one would obtain by expanding the inverse propagator to $O(q^2)$. The black dots correspond to the value of the order parameter at the turning points, where the pole is at $q^2 = 0$ and the scheme dependence disappears.

arises from ignoring the possible presence of contact terms in the two-point function, which pollute the result through the small- q^2 expansion.

Indeed, in general we expect that the analytic structure of the two-point function will include a collection of simple poles and finite contact terms:

$$\tilde{G}_0(\omega = 0, q) = \sum_i \frac{R_i}{q^2 - P_i} + \sum_j c_{2j} q^{2j}. \quad (4.25)$$

In the limit of low momenta and assuming that one of the poles dominates, meaning that it is sufficiently close to the origin compared to the rest, the relevant pieces of Eq. (4.25) are

$$\tilde{G}_0(\omega = 0, q) = \frac{R_0}{q^2 - P_0} + c_0 + c_2 q^2 + O(q^4). \quad (4.26)$$

Note that the contact terms c_0 and c_2 introduce non-localities in the effective action, since \tilde{G}_0^{-1} is no-longer a polynomial in q whenever they are present. In addition, they modify the low-momentum expansion of the inverse correlator to

$$\tilde{G}_0^{-1}(\omega = 0, q) = \frac{P_0}{c_0 P_0 - R_0} + \frac{R_0 - c_2 P_0^2}{(R_0 - c_0 P_0)^2} q^2 + O(q^4). \quad (4.27)$$

In our case, the agreement between the second derivative of the effective potential and $-A_0$, see Fig. 9 (left), tells us that $c_0 = 0$. On the other hand, c_2 depends on α , which would lead to a scheme-dependent kinetic term if one identified (4.27) with (4.15). However, this identification is not correct in the presence of contact terms, since the exact zero of the inverse correlator corresponds to the pole of the Green's function and this is scheme independent. In other words, the α -dependence is an artifact of the low-momentum expansion

$$2\varphi/(aT^3)$$

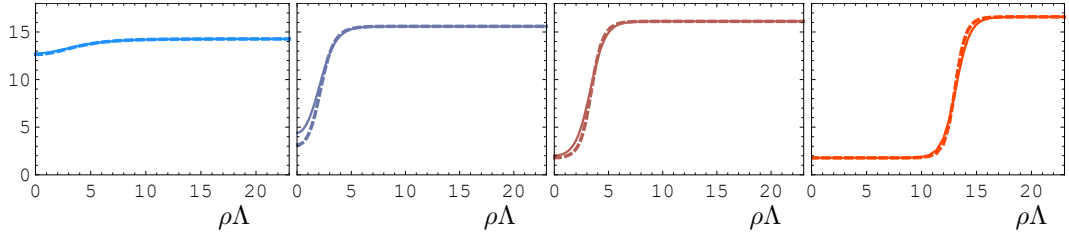


Figure 10: (Top) Comparison between the bubble profiles obtained from the microscopic holographic computation (solid) and the ones obtained from the effective action (dashed).

in the presence of contact terms. To avoid this problem, we identify the pole $q^2 = P_0$ of the Green's function that is closer to $q^2 = 0$ and compute directly the kinetic term using Eq. (4.18), which gives

$$Z(\varphi_0, T) = -\frac{\partial_\varphi^2 V_{\text{eff}}(\varphi_0, T)}{P_0}. \quad (4.28)$$

The mode that gives rise to this pole can be understood as follows. In the spinodal region, the sound mode is unstable at low momentum and stable at high momentum. Its dispersion relation takes the form of a parabola, as shown in e.g. Fig. 3 of [63]. By continuity, in the spinodal region there is a mode with

$$\omega = 0, \quad q^2 > 0. \quad (4.29)$$

The value of q^2 approaches zero as the turning point at $T = T_0$ is approached along the spinodal branch. Past this point, once in the metastable branch, this mode moves into the complex q -plane since now $q^2 < 0$. However, it remains closer to the origin than the rest of the poles and its residue gives the correct value of $Z(\varphi_0, T)$ through Eq. (4.18). The result is shown in red in Fig. 9 (right), overlaid on the α -dependent kinetic terms previously obtained from Eq. (4.24). As expected, $Z \sim a^{-1} \sim N^{-2}$. We find that Z exhibits a strong dependence on φ in the locally stable branches, i.e. outside the region delimited by the black dots, while it is approximately field-independent along the spinodal branch, corresponding to the region between these points. Moreover, in this region the magnitude of Z is suppressed by roughly three orders of magnitude relative to the naive dimensional estimate, $aZ \sim T^{-4}$. We will return to these features below.

We now have all the ingredients required to determine the critical bubbles by solving Eq. (4.3) for different values of the temperature. The results for the bubble profiles are shown in Fig. 10, where we see that the effective approach provides a remarkably accurate approximation to the exact result. The deviations become larger when the interior of the bubble corresponds to a state further away from the homogeneous equilibrium configurations, which is consistent with the fact that the effective action was derived by expanding around those states. Fig. 11 presents a similar comparison for the free energy excess, where once again a remarkable level of agreement is observed.

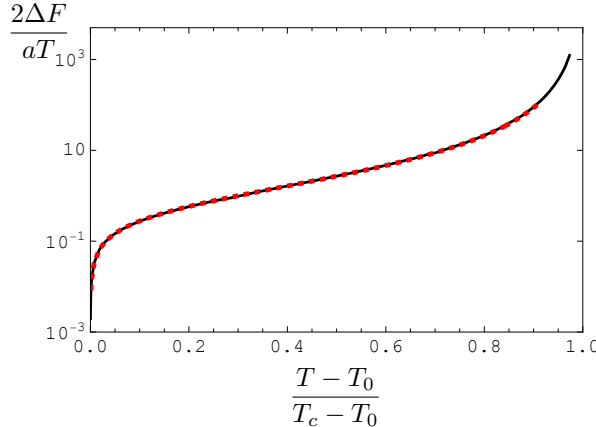


Figure 11: Comparison of the bubble action, as obtained from the microscopic computation (solid black) and from an effective action computed from first principles via holography (dashed red).

4.3 Phenomenological construction of the effective action

We have seen that when the two-derivative effective action (4.1) is known, it can be used to make accurate predictions about bubble properties, particularly the bubble action. However, in many cases of interest the effective action cannot be determined from first principles. In some instances, this is because the microscopic theory is unknown, as in Beyond the Standard Model scenarios. In other cases, the microscopic theory is known, but calculating the effective action is not feasible due to technical challenges, such as the strongly coupled nature of the physics. Despite these obstacles, progress can still be made by constructing an effective action motivated by a combination of phenomenological considerations and dimensional analysis. In this section, we will evaluate the accuracy of this approach in our case by comparing it to the microscopic description.

We begin with the effective potential. Renormalizability, together with the requirement to accommodate a FOPT, leads to an ansatz in the form of a degree-four polynomial—see e.g. [3, 5, 91]. For example, in the context of EW-like phase transitions, the order parameter is the expectation value of the Higgs field, $\langle \Phi_h \rangle$, and the potential is an expansion in powers of $\langle \Phi_h \rangle / T$ truncated at fourth order.

The requirement that the effective potential be consistent with the equation of state fixes the quartic polynomial. The expectation value of the order parameter, $\varphi = \langle \mathcal{O} \rangle$, is a multivalued function of the temperature across the phase transition. In particular, for temperatures in the range $T \in (T_0, T_c)$ it can take three distinct values, φ_+ , φ_s , and φ_- , corresponding to the metastable (+), spinodal (s), and stable (−) branches, respectively. Locally stable and unstable phases are associated with minima and maxima of the effective potential. Consequently, throughout the region of the FOPT, the potential must exhibit two minima separated by a single maximum. Moreover, the value of the potential at each of these extrema must coincide with the corresponding free energy density. We will therefore

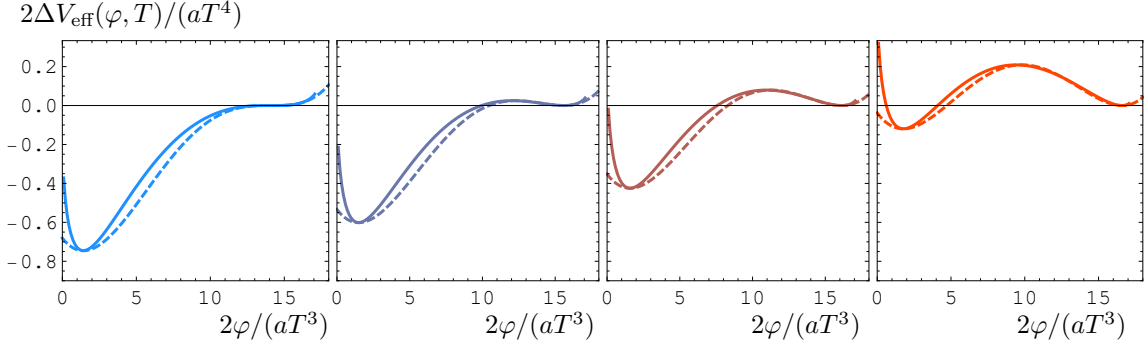


Figure 12: Comparison of the effective potentials shown in Fig. 8 (right) (solid curves), obtained directly from the quantum effective action, with their approximations using a degree-four polynomial (dashed curves).

impose

$$\begin{aligned} \partial_\varphi V_{\text{eff}}(\varphi, T) \Big|_{\varphi=\varphi_+} &= 0, & V_{\text{eff}}(T, \varphi_+) &= f_+, \\ \partial_\varphi V_{\text{eff}}(\varphi, T) \Big|_{\varphi=\varphi_-} &= 0, & V_{\text{eff}}(T, \varphi_-) &= f_-, \\ \partial_\varphi V_{\text{eff}}(\varphi, T) \Big|_{\varphi=\varphi_M} &= 0, & V_{\text{eff}}(T, \varphi_M) &= f_s. \end{aligned} \quad (4.30)$$

Note that we enforce the two minima of the potential to occur at the values of the order parameter φ_+ and φ_- determined by the equation of state. By contrast, for the maximum we only require that the value of the potential reproduces the free energy density of the spinodal branch, f_s , without fixing its location, namely, we do not impose $\varphi_M = \varphi_s$. Enforcing this additional condition would overconstrain the potential, since a quartic polynomial has only five independent parameters. This asymmetry is motivated by the fact that the locally stable states associated with the minima appear as asymptotic configurations of planar or large spherical bubbles, whereas the unstable state corresponding to the maximum does not. In Fig. 12, we compare the resulting degree-four polynomial potentials with those obtained from the quantum effective action, finding good agreement both qualitatively and quantitatively.

We now turn to the coefficient of the kinetic term in the effective action, $Z(\varphi, T)$. Unlike the effective potential, this cannot be determined from the equation of state. For this reason, simplifying assumptions are often made. The first one is that Z is approximately field-independent, i.e. that $Z(\varphi, T) \approx Z(T)$. In the spherically-symmetric case, we can then rescale the radial coordinate through

$$\rho = Z(T)^{1/2} \varrho \quad (4.31)$$

and rewrite the effective action (4.1) as

$$S_{\text{eff}}(T) = \frac{4\pi}{T} Z(T)^{3/2} \int_0^\infty d\varrho \varrho^2 \left(\frac{1}{2} (\partial_\varrho \varphi)^2 + V_{\text{eff}}(\varphi, T) \right). \quad (4.32)$$

Note that ϱ has dimensions of (energy)¹. This assumption simplifies the problem significantly because Z only appears as an overall multiplicative factor in the action. Conse-

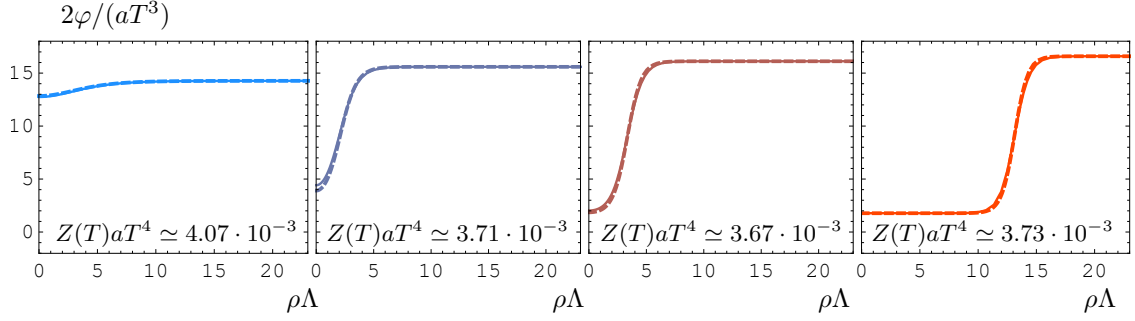


Figure 13: Profiles of the bubbles as a function of the radial coordinate for the order parameter $\varphi = \langle \mathcal{O} \rangle$. The four representatives shown correspond to the same temperatures as in the previous figures, see Fig. 4. The solid curves correspond to the result obtained from the full computation in the bulk, while the dashed ones are the result of the effective approach.

quently, the equation of motion becomes independent of Z :

$$\frac{d^2\varphi}{d\varrho^2} + \frac{2}{\varrho} \frac{d\varphi}{d\varrho} - \partial_\varphi V_{\text{eff}}(\varphi, T) = 0. \quad (4.33)$$

The net result is that we can determine the shape of the bubble profiles in the ϱ -coordinate without needing to know the normalization of the kinetic term. However, to obtain the overall physical size of the bubbles, i.e. their size in the ρ -coordinate, and to calculate the bubble action, which depends on the overall magnitude of $S_{\text{eff}}(T)$, the value of $Z(T)$ is required. The key point is that if the value of Z is determined from the microscopic theory, then excellent agreement with the microscopic results is found, thus justifying the assumption that Z is approximately field-independent. On the other hand, if Z can only be estimated using dimensional analysis, then a significant discrepancy arises.

To demonstrate this, we present the result of computing the bubble profiles in the ϱ -coordinate and then transforming them to the ρ -coordinate in Fig. 13. For this transformation we use the value of $Z(T)$ that yields the best fit to the microscopic profiles. This fitted value is shown in Fig. 14 (left), where we see that it is around

$$aZ \simeq 3.7 \times 10^{-3} T^{-4}. \quad (4.34)$$

This value agrees with that of $Z(\varphi, T)$ along the spinodal branch, corresponding to the region between the two black circles shown in Fig. 9 (right). The excellent agreement with the microscopic profiles seen in Fig. 13 confirms that a field-independent Z provides a good approximation, despite the fact that Z depends strongly on φ outside the spinodal branch. Presumably, the reason for this is that the kinetic term is only relevant in the region where gradients are large, i.e. across the bubble wall, and in this region the values of φ correspond to those in the spinodal branch. Fig. 14 shows that this procedure also yields an accurate prediction for the bubble action.

As mentioned earlier, in many relevant cases the coefficient Z cannot be determined from first principles. In such situations, one can attempt to estimate its approximate value

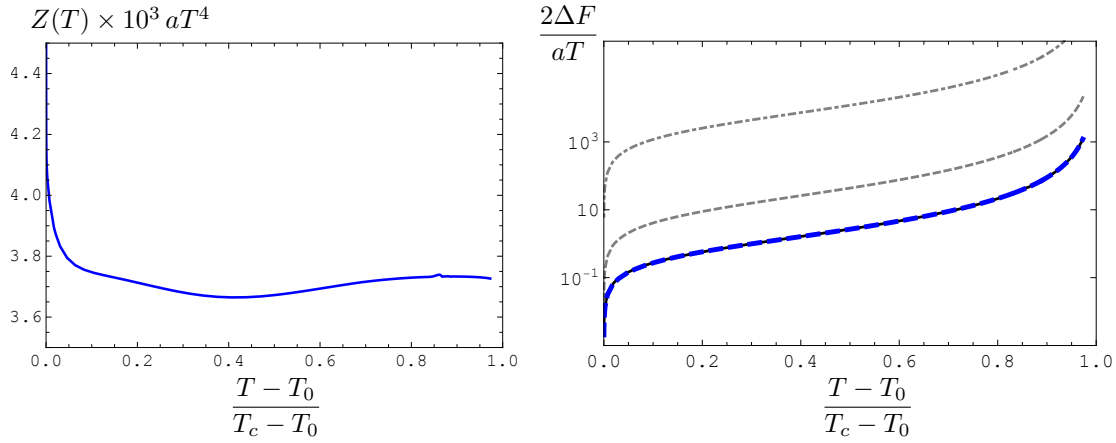


Figure 14: (Left) Coefficient of the kinetic term in the effective action with a degree-four polynomial that provides the best fit of the corresponding bubble profiles to those derived from the microscopic theory. (Right) Comparison between the bubble action obtained from the effective action with a degree-four polynomial (gray and blue curves) and the microscopic result (solid black curve). The dashed blue curve corresponds to the case where $Z(T)$ is fitted, as in the plot on the left. The gray dashed curve shows the result for the choice $aZ = \Lambda^{-4}$, while the dotted-dashed curve corresponds to $aZ = T^{-4}$.

using dimensional analysis. In our case, two natural choices are:

$$aZ \sim T^{-4} \quad (4.35)$$

or

$$aZ \sim \Lambda^{-4} \sim 2.5 \times 10^{-1} T^{-4}. \quad (4.36)$$

These estimates differ by 3 and 1 orders of magnitude, respectively, from the actual value derived from the microscopic theory—see Eq. (4.34). Since the bubble action scales as $S_{\text{eff}} \sim Z^{3/2}$, this discrepancy leads to significant differences between predictions based on the dimensional estimate of Z and those from the microscopic result, as shown in Fig. 14 (right).

The dimensional estimate can be substantially refined if additional information beyond the equation of state is available, specifically the surface tension. This is particularly useful given that the surface tension can be determined through lattice simulations as in Refs. [87, 88]. Recall that we introduced the notion of surface tension in Eq. (3.8) in the *thin wall approximation* (i.e. for large bubbles), where their structure can be decomposed into the excess free energy density (times the volume of the bubble) and a contribution from the wall:

$$\Delta S_{\text{eff}}(T) = \Delta S_{\text{inside}}(T) + S_{\text{wall}}(T). \quad (4.37)$$

In the effective theory, the first term is given by the difference in the effective potential,

$$\Delta S_{\text{inside}}(T) = \frac{4\pi R^3}{3T} \Delta V_{\text{eff}}(\varphi_-, T), \quad (4.38)$$

with $\Delta V_{\text{eff}}(\varphi, T)$ defined by Eq. (4.22). Here, we will focus our attention on the contribution from the wall.

In the large bubble regime in which the current analysis is applicable, the second term in the equation of motion (4.33) is suppressed by the radius of the bubble, and thus negligible. Then

$$\frac{d^2\varphi}{d\varrho^2} \simeq \partial_\varphi V_{\text{eff}}(\varphi, T) \quad \Rightarrow \quad \frac{1}{2} \left(\frac{d\varphi}{d\varrho} \right)^2 \simeq \Delta V_{\text{eff}}(\varphi, T), \quad (4.39)$$

where to get the second expression we have multiplied by $\partial_\varrho \varphi$ and integrated over ϱ from infinity. Denoting the size of the bubble in the ϱ -coordinate by $\varrho_b \equiv R Z(T)^{-1/2}$, we can use Eq. (4.39)—steps (i) and (iii)—and the fact that ϱ_b is almost constant in the region of the wall together with a change of variables—step (ii)—to evaluate

$$\begin{aligned} S_{\text{wall}}(T) &= \frac{4\pi}{T} Z(T)^{3/2} \int_{\varrho_b-\delta}^{\varrho_b+\delta} d\varrho \varrho^2 \left(\frac{1}{2} (\partial_\varrho \varphi)^2 + \Delta V_{\text{eff}}(\varphi, T) \right) \\ &\stackrel{(i)}{\simeq} \frac{4\pi}{T} Z(T)^{3/2} \int_{\varrho_b-\delta}^{\varrho_b+\delta} d\varrho \varrho^2 (\partial_\varrho \varphi)^2 \\ &\stackrel{(ii)}{\simeq} \frac{4\pi}{T} Z(T)^{1/2} R^2 \int_{\varphi_-}^{\varphi_+} d\varphi \partial_\varrho \varphi \\ &\stackrel{(iii)}{\simeq} \frac{4\pi}{T} Z(T)^{1/2} R^2 \int_{\varphi_-}^{\varphi_+} d\varphi \sqrt{2\Delta V_{\text{eff}}(\varphi, T)} \\ &\equiv \frac{4\pi R^2}{T} \sigma. \end{aligned} \quad (4.40)$$

The expressions above should be understood in the limit $\delta \rightarrow 0$ and $R \rightarrow \infty$. The latter ensures that the two minima, φ_+ and φ_- , of the effective potential become exactly degenerate, and that the potential difference $\Delta V_{\text{eff}}(\varphi, T)$, appearing under the square root, remains strictly positive between them. Thus, in the effective theory the surface tension can be expressed as

$$\sigma = Z(T_c)^{1/2} \int_{\varphi_-}^{\varphi_+} d\varphi \sqrt{2\Delta V_{\text{eff}}(\varphi, T_c)}. \quad (4.41)$$

At T_c the two homogeneous solutions share the same value for the free energy density,

$$f_+ = f_- \equiv f_c, \quad (4.42)$$

in which case the conditions in Eq. (4.30) imply that

$$\Delta V_{\text{eff}}(\varphi, T_c) = 16(f_s - f_c) \frac{(\varphi - \varphi_+)^2(\varphi - \varphi_-)^2}{(\varphi_+ - \varphi_-)^4}. \quad (4.43)$$

Substituting in (4.41) we arrive at

$$\sigma = Z(T_c)^{1/2} \frac{2\sqrt{2}}{3} |\Delta\varphi| \sqrt{f_s - f_c}. \quad (4.44)$$

with $\Delta\varphi = \varphi_- - \varphi_+$. In our case σ is given in Eq. (3.12) and we can read off from Fig. 8(right) that

$$\Delta V_{\text{eff}}(\varphi_M, T_c) = f_s - f_c \simeq 1.35 \times 10^{-1} a T_c^4, \quad |\Delta\varphi| \simeq 7.42 a T_c^3. \quad (4.45)$$

Substituting in (4.44) and solving for $Z(T_c)$ gives

$$aZ \simeq 3.66 \times 10^{-3} T_c^{-4}, \quad (4.46)$$

which is remarkably close to the values that provide the best fit depicted in Fig. 14, see also Eq. (4.34). Moreover, as in Eq. (3.13), the scaling of the bubble action deviates from the standard result $\Delta F \propto (T - T_0)^{3/2}$ found in Ref. [81]. The agreement between our microscopic result and the effective description based on a quartic polynomial with a constant kinetic term suggests that this discrepancy is not a consequence of the different approaches (microscopic vs effective), nor of the assumption that $Z(\varphi, T)$ is constant. Rather, we trace it to the way the effective potential develops an inflection point. Indeed, while in Ref. [81] some coefficients of the effective potential vanish at the spinodal point, in our case all of them remain finite. It would be interesting to characterize the different exponents that one could get with a degree four polynomial, which we leave for future work.

We conclude that requiring the effective action to reproduce the correct surface tension provides an accurate estimate of the kinetic term. As we have seen, under these conditions the effective action then reproduces the bubble properties with high precision.

5 Conclusions

In this work we have presented a fully microscopic description of critical bubbles in a strongly coupled, four-dimensional gauge theory undergoing a first-order thermal phase transition. Using holography, we constructed static, inhomogeneous, and unstable black-brane solutions dual to $O(3)$ -symmetric critical bubbles in the boundary theory. The explicit construction of these geometries allowed us to compute key properties of the critical bubbles directly from the microscopic theory across the entire metastable branch, including the bubble profile, the surface tension and the nucleation rate. From the bulk perspective, these quantities are encoded in localized deformations of the black-brane horizon, providing a geometric interpretation of the bubble properties.

A central goal of this work was to assess the validity of effective descriptions of first-order phase transitions. To this end, we compared our microscopic results with those obtained from a two-derivative effective action for the order parameter in two distinct scenarios. When the effective action was derived holographically from first principles, we found remarkable agreement with the microscopic results for the bubble profiles, surface tension, and nucleation rates. This provides strong evidence that, when properly constructed, effective actions can faithfully capture even highly inhomogeneous and intrinsically non-perturbative configurations such as critical bubbles.

In contrast, when the effective action is constrained solely by the equation of state and dimensional analysis, substantial discrepancies emerge. In particular, in our theory this approach significantly overestimates the coefficient of the kinetic term, leading to incorrect bubble properties and nucleation rates. We showed that these discrepancies can be traced to a suppression of the surface tension relative to naive dimensional expectations. Imposing the correct surface tension as an additional constraint on the effective action is sufficient to

restore agreement with the microscopic results. Interestingly, lattice studies [87, 88] have observed similar behavior in the deconfinement transition of large- N $SU(N)$ Yang–Mills theories, implying markedly less supercooling than naïvely expected [89]. While this parallel is suggestive, it should be interpreted with caution, as in our case the transition takes place between two deconfined phases rather than between confined and deconfined phases.

Several extensions of this work are natural. A particularly interesting one is the computation of the fluctuation determinant around the critical bubble, which controls the prefactor of the nucleation rate. Within the holographic framework, this problem can be naturally addressed by analyzing the spectrum of quasinormal modes of the corresponding inhomogeneous black-brane geometries [92]. Such a calculation would yield a fully microscopic determination of both the exponential suppression and the prefactor of the nucleation rate at strong coupling.

It would also be interesting to investigate whether a similar suppression of the surface tension occurs in other strongly coupled theories, and to what extent these insights can inform phenomenological models of cosmological or astrophysical first-order phase transitions. We expect that the framework developed here will provide a valuable benchmark for future studies of phase transitions beyond the reach of perturbative methods.

Acknowledgements

We thank Alessio Caddeo, Jorge Casalderrey-Solana, Oliver Gould, Oscar Henriksson, Niko Jokela, Tomislav Prokopec, Ronnie Rodgers, Mikel Sanchez-Garitaonandia, Pedro Tarancón-Alvarez, Jorinde van de Vis and Miguel Vanvlasselaer for useful discussions. JS thanks Tomas Andrade, Alexander Krikun and Christiana Pantelidou for guidance in learning how to solve PDEs with pseudospectral methods. D.M. acknowledges financial support from Grant CEX2024-001451-M funded by MICIU-AEI-10.13039/501100011033, from Grant No. PID2022-136224NB-C22 from the Spanish Ministry of Science, Innovation and Universities, and from Grant No. 2021-SGR-872 funded by the Catalan Government. C.H. is partially supported by the Spanish Agencia Estatal de Investigación and Ministerio de Ciencia, Innovación y Universidades through the grants PID2021-123021NB-I00 and PID2024-161500NB-I00. This research is also funded by the European Union (ERC, HoloGW, Grant Agreement No. 101141909). Views and opinions expressed are, however, those of the authors only and do not necessarily reflect those of the European Union or the European Research Council. Neither the European Union nor the granting authority can be held responsible for them.

A Numerical Implementation

In this Appendix we provide further details about how we solved the system of PDEs.

To gain some handle on the numerical solutions and their precision, we performed some variable and coordinate redefinitions. First, note that in the UV expansion of the functions $Q_i(z, \rho)$ (see Eq. (2.21)) the coefficients that have to be extracted from the numerical solution appear at relatively high order. In particular, we would need to take a fourth

order derivative to compute them. Differentiating a numerical solution so many times introduce large numerical errors. For this reason, we preferred to solve the system of equations in terms of a new set of variables q_i , defined by

$$\begin{aligned} Q_i(\rho, z) &= 1 + z^3 q_i(\rho, z), \quad \text{for } i \in \{1, 2, 3, 4\} \\ Q_5(\rho, z) &= z^4 q_5(\rho, z), \\ Q_0(\rho, z) &= 1 + z q_0(\rho, z). \end{aligned} \tag{A.1}$$

In terms of these, the UV boundary conditions are simply $q_i(z, x) = 0$, and the unknown coefficients are given in terms of first derivatives with respect to z . On the other hand, the new variables satisfy mixed boundary conditions at the horizon.

In addition, it is also convenient to compactify the ρ coordinate, for which we introduce a general coordinate change $\rho = \rho(x)$, with $x \in [0, 1]$. The concrete form of $\rho(x)$ is adapted to the expected properties of each solution. For instance, for small bubbles (i.e. temperatures close to the spinodal point T_0), a convenient choice is

$$\rho(x) = \rho_1(x) \equiv \frac{ax}{1 - x^2}, \tag{A.2}$$

for some $a \in \mathbb{R}$. This coordinate is helpful for bubbles for which the non-trivial, varying part of the solution is within a region close to the origin of a characteristic size a , as it happens for temperatures close to T_0 . For each solution we adjust the value of the parameter a .

As the wall develops, we considered the more suitable yet involved coordinate change

$$\rho(x) = \rho_2(x) \equiv \frac{ax (d_0 + 3\tau_0^2 - 3\tau_0 + 1) (d_0 + 3\tau_0^2 + x^2 - 3\tau_0 x)}{x^2 (d_0 + 3\tau_0^2 + x^2 - 3\tau_0 x)^2 - (d_0 + 3\tau_0^2 - 3\tau_0 + 1)^2}. \tag{A.3}$$

This coordinate and the corresponding choice of a , d_0 and τ_0 are engineered so that the relevant region of the solution is zoomed in, at the same time that the wall is located around $x \simeq 1/2$. Note that $\rho_2(x) = \rho_1(d_0(x - \tau_0) + (x - \tau_0)^3 + d_0\tau_0 + \tau_0^3)$.

Finally, for sufficiently large bubbles (close to the critical temperature T_c) the latter choice also ceases to be convenient. But we know that in this regime the solution is approximately homogeneous everywhere except close to the wall and, in particular, its profile is well approximated by a hyperbolic tangent. For this reason we choose the change

$$\rho(x) = \rho_3(x) = \rho_0 + w_0 \operatorname{artanh} \left(x + (x - 1) \tanh \left(\frac{\rho_0}{w_0} \right) \right), \tag{A.4}$$

designed to zoom in the relevant region of width w_0 around the radius ρ_0 . The values of these parameters are calculated using the fits to a hyperbolic tangent in Eq. (3.3) from previously found solutions and extrapolating to the next, with⁵ $\rho_0 = R$ and $w_0 = \ell$. There is however a subtlety in the coordinate choice defined by Eq. (A.4). Note that $\rho_3(x)$ is almost vertical at the origin, which makes it numerically challenging to impose Neumann

⁵In hindsight, it would have probably been even better to choose $w_0 = m \cdot \ell$, with m some number between 2 and $\rho_0/2$, in such a way that the coordinate does not zooms in only the wall but also a small region around it. Nevertheless, our choice worked well enough in our case.

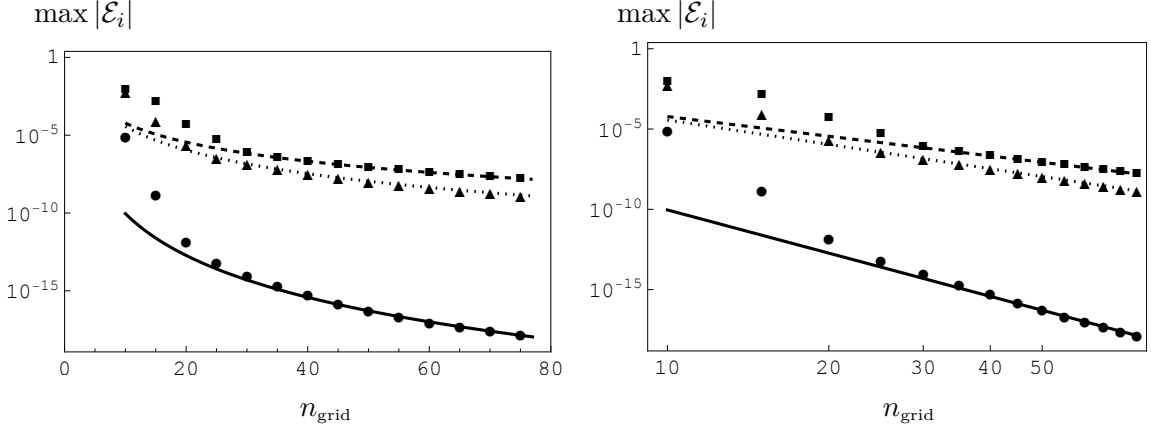


Figure 15: Maximum absolute value of the different components of ξ_A , properly normalized, as a function of the number of grid points in every directions ($n_{\text{grid}} = n_x = n_z$). These plots show that spectral convergence is spoiled in our case, probably due to the presence of the logarithms near the boundary. The curves show fits for \mathcal{E}_1 (circles, solid curve), \mathcal{E}_2 (squares, dashed curve) and \mathcal{E}_3 (triangles, dotted curve) to $\max |\mathcal{E}_i| = K_i(n_{\text{grid}})^{a_i}$ using the last six last data points shown.

boundary conditions there. Fortunately, when this choice becomes the convenient one, the solution at the origin is so close to the corresponding homogeneous stable state that it is possible to switch to Dirichlet boundary conditions there.

In contrast, we did not need to perform any change of variables along the z coordinate. Practically, we set $z_{\text{H}} = 1$, which implies that all quantities extracted from our numerical solution are expressed in units of z_{H} . Equivalently, this amounts to working with the coordinate $\mathbf{z} = z/z_{\text{H}}$.

After all these definitions, we are left with a system of six second order PDEs defined in $(x, z) \in [0, 1] \times [0, 1]$. We used Chebyshev grids in both directions, with n_x and n_z points respectively, including the boundaries. This allowed us to solve the problem with grids of moderate size. However, the method is limited for two reasons. On the one hand, note the appearance of logarithms in our asymptotic expansions, Eq. (2.21), which spoil spectral convergence. Convergence is also limited by the development of the bubble wall, but this is cured by the different choices of coordinates introduced earlier. These two issues forced us to work with precision higher than `MachinePrecision`, which is easily implemented in Mathematica. For most of the bubbles that we constructed, $n_z = 50$ and $n_x = 50$ or 80 , even though we checked robustness of the results by computing some of them again in a 70×70 grid. In most cases, we computed the reference metric with 80 digits of precision and solved the system of PDEs with 60 digits of precision, using a Newton-Raphson procedure, see Ref. [93].

In addition, the evaluation of the De Turk vector ξ_A gives us a way to check the convergence of our implementation. Recall that the only non-vanishing components of ξ_A as defined in Eq. (2.15) were ξ_ρ and ξ_z . Analyzing how these approach $\rho = 0$ and $\rho \rightarrow \infty$, we realized that it is convenient to define the quantities

$$(\mathcal{E}_1, \mathcal{E}_2, \mathcal{E}_3) = \left(\begin{array}{l} \rho^2 \xi_A \xi^A, \quad \rho \xi_\rho, \quad (z_{\text{H}} + \rho) \xi_z \end{array} \right), \quad (\text{A.5})$$

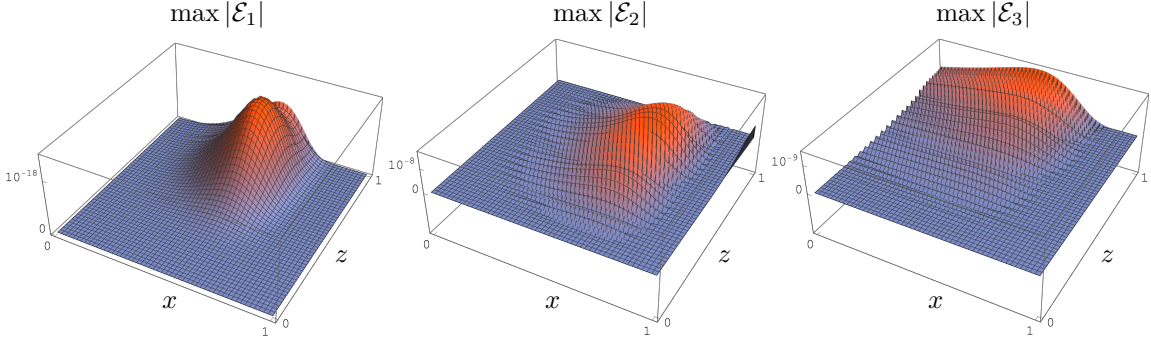


Figure 16: Plot of the quantities defined on Eq. (A.5) for $n_{\text{grid}} = 75$.

where the additional factors of ρ make sure that the corresponding \mathcal{E}_i approach the origin and infinity *off-shell* as

$$\mathcal{E}_i = \mathbf{e}_{i,0}(z) + O(\rho), \quad \mathcal{E}_i = \mathbf{e}_{i,\infty}(z) + O(\rho^{-1}). \quad (\text{A.6})$$

B Holographic Renormalization

In this Appendix, we collect the formulas for the renormalized expectation values of the holographic energy-momentum tensor and the scalar operator, obtained after performing the holographic renormalization procedure (see Refs. [85, 94, 95]). We follow the structure of Appendix B in Ref. [96], with the caveat that $\rho|_{\text{there}} = \tilde{z}^2|_{\text{here}}$. The starting point is to write the metric in FG coordinates, as in Eq. (2.9), which we copy here for ease of reference,

$$ds^2 = \frac{L^2}{\tilde{z}^2} \left(d\tilde{z}^2 + g_{\mu\nu}(\tilde{z}, x) dx^\mu dx^\nu \right). \quad (\text{see (2.9)})$$

Recall that the boundary is located at $\tilde{z} = 0$. For any gravity theory defined by Eq. (2.1) and whose potential behaves close to the origin as Eq. (2.4), the metric and the scalar field approach the boundary as

$$\begin{aligned} g_{\mu\nu}(\tilde{z}, x) &= \frac{L^2}{\tilde{z}^2} \left(\gamma_{\mu\nu}(x) + \gamma_{(2)\mu\nu}(x) \tilde{z}^2 + \left(\gamma_{(4)\mu\nu}(x) + h_{(4)\mu\nu}(x) \log \tilde{z} \right) \tilde{z}^4 + O(\tilde{z}^6) \right), \\ \phi(\tilde{z}, x) &= \tilde{z} \left(\phi_{(0)}(x) + \left(\phi_{(2)}(x) + \psi_{(2)}(x) \log \tilde{z} \right) \tilde{z}^2 + O(\tilde{z}^4) \right). \end{aligned}$$

Four of the coefficients we just wrote are not fixed by the asymptotic analysis of the equations. Two of these are the leading orders coefficients $\gamma_{\mu\nu}(x)$ and $\phi_{(0)}(x)$, which correspond to the boundary metric and the source of the operator dual to ϕ , respectively. In our paper, $\gamma_{\mu\nu}(x) = \eta_{\mu\nu}$ was always fixed to flat Minkowski metric, while⁶ $\phi_{(0)}(x) = \Lambda + J(x)$. We will nevertheless keep the expressions in this Appendix general. While the asymptotic analysis imposes two conditions that the components of $\gamma_{(4)\mu\nu}(x)$ need to satisfy, the remaining freedom and the coefficient $\phi_{(2)}(x)$ are only fixed after specifying regularity conditions in

⁶With $J = 0$ in Section 2.

the bulk (in our case, the presence of a regular horizon). The rest of the terms in Eq. (B.1) are given in terms of the two leading ones,

$$\begin{aligned}\psi_{(2)} &= -\frac{1}{4} \left(\bar{\square} \phi_{(0)} - \frac{1}{6} \phi_{(0)} \bar{R} \right), \quad \gamma_{(2)\mu\nu} = -\frac{1}{2} \left(\bar{R}_{\mu\nu} - \frac{1}{6} \bar{R} \gamma_{\mu\nu} \right) - \frac{\phi_{(0)}^2}{3} \gamma_{\mu\nu}, \\ h_{(4)\mu\nu} &= h_{(4)\mu\nu}^{\text{grav}} - \frac{1}{12} \bar{R}_{\mu\nu} \phi_{(0)}^2 - \frac{1}{3} \bar{\nabla}_\mu \phi_{(0)} \bar{\nabla}_\nu \phi_{(0)} + \frac{1}{12} \bar{\nabla}_\sigma \phi_{(0)} \bar{\nabla}^\sigma \phi_{(0)} \gamma_{\mu\nu} + \frac{1}{6} \phi_{(0)} \bar{\nabla}_\mu \bar{\nabla}_\nu \phi_{(0)} \\ &\quad + \frac{1}{12} \phi_{(0)} \bar{\square} \phi_{(0)} \gamma_{\mu\nu},\end{aligned}\tag{B.1}$$

where the bars indicate that the corresponding geometrical quantity is computed with respect to the boundary metric $\gamma_{\mu\nu}$, and

$$\begin{aligned}h_{(4)\mu\nu}^{\text{grav}} &= \frac{1}{8} \bar{R}_{\mu\sigma\nu\tau} \bar{R}^{\sigma\tau} - \frac{1}{48} \bar{\nabla}_\mu \bar{\nabla}_\nu \bar{R} + \frac{1}{16} \bar{\square} \bar{R}_{\mu\nu} - \frac{1}{24} \bar{R} \bar{R}_{\mu\nu} \\ &\quad + \left(\frac{1}{96} \bar{R}^2 - \frac{1}{96} \bar{\square} \bar{R} - \frac{1}{32} \bar{R}_{\sigma\tau} \bar{R}^{\sigma\tau} \right) \gamma_{\mu\nu}.\end{aligned}\tag{B.2}$$

Now, the renormalized action of our holographic model contains three pieces:

$$I_{\text{ren}} = I_g + I_{\text{GHY}} + I_{\text{ct}}.\tag{B.3}$$

The first term is the bulk action Eq. (2.1), while the second one is the usual Gibbons-Hawking-York (GHY) boundary term included to have a well posed variational problem,

$$I_{\text{GHY}} = \frac{1}{\kappa_5^2} \int d^4x \sqrt{-h} K,\tag{B.4}$$

with h the determinant of $h_{\mu\nu}$ the induced metric on a constant $\tilde{z} = \epsilon_{\text{UV}}$ four-dimensional slice near the boundary. At the end of the computation we take $\epsilon_{\text{UV}} \rightarrow 0$. Moreover, $K = h^{\mu\nu} K_{\mu\nu}$ is the trace of the extrinsic curvature $K_{\mu\nu}$ of the four-dimensional slice. Finally,

$$\begin{aligned}I_{\text{ct}} &= \frac{2}{\kappa_5^2} \int d^4x \sqrt{-h} \left[-\frac{\tilde{R}L}{8} - \frac{3}{2L} + \left(\frac{L^3}{16} \left(\tilde{R}_{\mu\nu} \tilde{R}^{\mu\nu} - \frac{1}{3} \tilde{R}^2 \right) + \frac{L}{2} \left(\phi \tilde{\square} \phi - \frac{1}{6} \tilde{R} \phi^2 \right) \right) \log \epsilon_{\text{UV}} \right. \\ &\quad \left. + \alpha \mathcal{A} L^3 + \beta \frac{\phi^4}{L} \right]\end{aligned}\tag{B.5}$$

is a counter-term defined on the $\tilde{z} = \epsilon_{\text{UV}}$ hypersurface which makes I_{ren} finite when the limit $\epsilon_{\text{UV}} \rightarrow 0$ is taken. In this expression the tildes indicate that the corresponding geometric quantities are computed using the metric $h_{\mu\nu}$. Actually, the two last terms accompanied by the constants α and β are finite and stand for residual renormalization-scheme ambiguities of the model. The first one is proportional to the holographic conformal anomaly [82, 97] $\mathcal{A} = \mathcal{A}_g + \mathcal{A}_\phi$ consisting of a gravitational part due to the curved boundary geometry and a part due to scalar matter

$$\mathcal{A}_g = \frac{1}{16} (\bar{R}^{\mu\nu} \bar{R}_{\mu\nu} - \frac{1}{3} \bar{R}^2), \quad \mathcal{A}_\phi = -\frac{1}{2} \left(\bar{\nabla}_\sigma \phi_{(0)} \bar{\nabla}^\sigma \phi_{(0)} + \frac{1}{6} \bar{R} \phi_{(0)}^2 \right).\tag{B.6}$$

The second one plays the role of a vacuum energy.

With all this information, we can give an expression for the expectation value of the boundary stress tensor,

$$\begin{aligned} \langle T_{\mu\nu}^{\text{QFT}} \rangle &= \frac{2}{\sqrt{-\gamma}} \frac{\delta I_{\text{ren}}}{\delta \gamma^{\mu\nu}} \\ &= \frac{2L^3}{\kappa_5^2} \left[\gamma_{(4)\mu\nu} + \frac{1}{8} \left(\text{Tr} \gamma_{(2)}^2 - (\text{Tr} \gamma_{(2)})^2 \right) \gamma_{\mu\nu} - \frac{1}{2} \gamma_{(2)}^2 + \frac{1}{4} \gamma_{(2)\mu\nu} \text{Tr} \gamma_{(2)} + \frac{1}{2} \bar{\nabla}_\mu \phi_{(0)} \bar{\nabla}_\nu \phi_{(0)} \right. \\ &\quad \left. + \left(\phi_{(0)} \phi_{(2)} - \frac{1}{2} \phi_{(0)} \psi_{(2)} - \frac{1}{4} \bar{\nabla}_\sigma \phi_{(0)} \bar{\nabla}^\sigma \phi_{(0)} \right) \gamma_{\mu\nu} + \alpha \left(\mathcal{T}_{\mu\nu}^\gamma + \mathcal{T}_{\mu\nu}^\phi \right) + \left(\frac{1}{18} + \beta \right) \phi_{(0)}^4 \gamma_{\mu\nu} \right], \end{aligned} \quad (\text{B.7})$$

with the anomalous contributions given by

$$\begin{aligned} \mathcal{T}_{\mu\nu}^g &= 2h_{(4)\mu\nu}, \\ \mathcal{T}_{\mu\nu}^\phi &= -\frac{1}{6} \phi_{(0)}^2 \bar{R}_{\mu\nu} - \frac{2}{3} \bar{\nabla}_\mu \phi_{(0)} \bar{\nabla}_\nu \phi_{(0)} + \frac{1}{6} \bar{\nabla}_\sigma \phi_{(0)} \bar{\nabla}^\sigma \phi_{(0)} \gamma_{\mu\nu} + \frac{1}{3} \phi_{(0)} \bar{\nabla}_\mu \bar{\nabla}_\nu \phi_{(0)} \\ &\quad - \frac{1}{3} \phi_{(0)} \bar{\square} \phi_{(0)} \gamma_{\mu\nu} + \frac{1}{12} \bar{R} \phi_{(0)}^2 \gamma_{\mu\nu}. \end{aligned} \quad (\text{B.8})$$

Similarly, the expectation value of the operator dual to ϕ is

$$\langle \mathcal{O} \rangle = \frac{1}{\sqrt{-\gamma}} \frac{\delta S_{\text{hol}}}{\delta \phi_{(0)}} = \frac{2L^3}{\kappa_5^2} \left[(1 - 4\alpha) \psi_{(2)} - 2\phi_{(2)} - 4\beta \phi_{(0)}^3 \right], \quad (\text{B.9})$$

and the anomaly-corrected Ward identities

$$\bar{\nabla}^\mu \langle T_{\mu\nu}^{\text{QFT}} \rangle = -\langle \mathcal{O} \rangle \bar{\nabla}_\nu \phi_{(0)}, \quad \gamma^{\mu\nu} \langle T_{\mu\nu}^{\text{QFT}} \rangle = -\phi_{(0)} \langle \mathcal{O} \rangle + \frac{2L^3}{\kappa_5^2} (\mathcal{A}_g + \mathcal{A}_\phi), \quad (\text{B.10})$$

are satisfied.

C Free energy

In this Appendix we show that the on-shell action, which provides the value of the free energy, can be computed as in Eq. (2.37). We start by showing different identities we will employ.

C.1 Useful expressions

The bubble solutions constructed in this work possess a hypersurface-orthogonal timelike Killing field ζ^A . This means that,

$$\nabla_{(A} \zeta_{B)} = 0, \quad \zeta_{[A} \nabla_{B]} \zeta_C = 0. \quad (\text{C.1})$$

In our coordinates —Eqs. (2.9) and (2.18)— this vector field is just $\zeta = \partial_t$. In addition, our geometries have a (inhomogeneous) Killing horizon, generated by ζ^A on the hypersurface where its norm vanishes.

Denoting the norm of the Killing vector as $\zeta^2 \equiv g_{AB}\zeta^A\zeta^B$, and defining $Z = \sqrt{-\zeta^2}$, we can find two useful expressions involving covariant derivatives of ζ^A along its integral curves,

$$\begin{aligned}\zeta^B\nabla_B\zeta_A &= -\zeta^B\nabla_A\zeta_B = -\frac{1}{2}\nabla_A(\zeta^2) = \frac{1}{2}\nabla_A(Z^2) = Z\nabla_A(Z), \\ \zeta^B\nabla_B(Z) &= \frac{1}{2Z}\zeta^B\nabla_B(Z^2) = -\frac{1}{2Z}\zeta^B\nabla_B(\zeta^C\zeta_C) = -\frac{1}{Z}\zeta^B\zeta^C\nabla_B\zeta_C = 0.\end{aligned}\tag{C.2}$$

Some of the expressions that we will find later will involve the future directed unit vector field $u^A \equiv \zeta^A/\sqrt{-\zeta^2} = \zeta^A/Z$, whose acceleration vector $a^A \equiv u^B\nabla_Bu^A$ satisfies the important property

$$a_A = u^B\nabla_Bu_A = u^B\nabla_B\left(\frac{\zeta_A}{Z}\right) = \frac{1}{Z^2}\zeta^B\nabla_B\zeta_A - \frac{1}{Z^3}\zeta^B\zeta_A\nabla_B(Z) = \frac{1}{Z}\nabla_A(Z).\tag{C.3}$$

In the last step we used the two identities in Eq. (C.2).

So far we have only used that ζ^A is Killing. Contracting the hypersurface orthogonality condition $\zeta_{[A}\nabla_{B]\zeta_C} = 0$ with ζ^C we obtain

$$\zeta^C\zeta_A\nabla_B\zeta_C + \zeta^C\zeta_B\nabla_C\zeta_A - Z^2\nabla_A\zeta_B = 0.\tag{C.4}$$

This, in turn, can be rewritten as

$$\nabla_A\zeta_B = a_A\zeta_B - a_B\zeta_A\tag{C.5}$$

making use of Eqs. (C.2) and (C.3). Using this expression, together with Eq. (C.3), we obtain the last property that we will use later,

$$\nabla_A\left(\frac{\zeta_B}{\zeta^2}\right) = -\nabla_A\left(\frac{\zeta_B}{Z^2}\right) = -\frac{1}{Z^2}\nabla_A\zeta_B + \frac{2}{Z^3}\zeta_B\nabla_AZ = \frac{1}{Z^2}(a_A\zeta_B + a_B\zeta_A).\tag{C.6}$$

C.2 Evaluation of the on-shell action

With the previous expressions at hand, let us evaluate Eq. (B.3) on our solutions. We focus our attention first on the bulk integral I_g , explicitly written in Eq. (2.1). After several steps we will be able to show that its integrand can be written as a total derivative. Start by reordering Einstein's equations as

$$g_{MN}R = -2(T_{MN} - R_{MN}) = -2\left(2\partial_M\phi\partial_N\phi - g_{MN}\left((\partial_A\phi\partial^A\phi + 2V(\phi))\right) - R_{MN}\right).\tag{C.7}$$

As a consequence, projecting onto ζ^A we obtain

$$R = 2\left((\partial_A\phi\partial^A\phi + 2V(\phi))\right) + \frac{2}{\zeta^2}\zeta^A\zeta^BR_{AB},\tag{C.8}$$

where we have used that $\zeta^A\partial_A\phi = \zeta^A\nabla_A\phi = 0$. Substituting this expression into the integrand of the bulk action I_g in Eq. (2.1), we discover that it can be expressed in terms of derivatives of the Killing vector,

$$\frac{R}{4} - \frac{1}{2}\partial_A\phi\partial^A\phi - V(\phi) = \frac{1}{2\zeta^2}\zeta^A\zeta^BR_{AB} = -\frac{1}{2\zeta^2}\zeta_B\nabla_A\nabla^A\zeta^B,\tag{C.9}$$

In the last identity we have used that, since ζ^A is Killing, $\nabla_A \nabla^A \zeta^B = -R^B_A \zeta^A$.

Now we would like to express Eq. (C.9) as a total derivative, so that we can use Stokes' theorem to perform the integral. Integration by parts results into

$$-\frac{1}{2\zeta^2} \zeta_B \nabla_A \nabla^A \zeta^B = -\frac{1}{2} \left[\nabla_A \left(\frac{\zeta_B}{\zeta^2} \nabla^A \zeta^B \right) - \nabla_A \left(\frac{\zeta_B}{\zeta^2} \right) \nabla^A \zeta^B \right]. \quad (\text{C.10})$$

Importantly, the second term inside the squared parenthesis is the contraction of the antisymmetric expression in Eq. (C.5) with the symmetric one from Eq. (C.6). Therefore, that term vanishes in our case and the integrand in I_g is indeed a total derivative. As a consequence we can use Stokes' theorem and write

$$I_g = \frac{2}{\kappa_5^2} \int d^5x \sqrt{-G} \nabla_A \left(-\frac{\zeta_B}{2\zeta^2} \nabla^A \zeta^B \right) = -\frac{1}{\kappa_5^2} \sum_i \int \left(\frac{\zeta_B}{\zeta^2} \nabla^A \zeta^B \right) d\Sigma_A^{(i)}. \quad (\text{C.11})$$

Here the sum runs over the different boundaries, with $d\Sigma_A^{(i)}$ denoting each directed hypersurface volume element. For spacelike or timelike boundaries,

$$d\Sigma_A^{(i)} \equiv n_A^{(i)} \sqrt{|h^{(i)}|} d^4y \equiv n_A^{(i)} dV^{(i)}, \quad (\text{C.12})$$

with $dV^{(i)}$ the induced volume element, $n_A^{(i)}$ the outward unit normal, and $h^{(i)}$ the determinant of the induced metric on the boundary,

$$h_{MN}^{(i)} = g_{MN} - s n_M^{(i)} n_N^{(i)}, \quad s \equiv n_A n^A = \pm 1. \quad (\text{C.13})$$

In our solutions, there are only two boundaries contributing to Eq. (C.11), the asymptotic AdS boundary and the horizon, $I_g = I_\infty + I_H$. Note that the horizon is a null hypersurface. As a consequence, we cannot use Eqs. (C.12) and (C.13) directly. Rather, we will consider a family of timelike surfaces and take the limit in which this family approaches the horizon. Also, to simplify the notation, we use the labels $i = \infty$ at the boundary of AdS and $i = H$ for the family of hypersurfaces close to the horizon. Moreover, we denote the corresponding outward unit normals as $n_A \equiv n_A^{(\infty)}$ and $m_A \equiv n_A^{(H)}$.

The boundary of AdS is the hypersurface at $z = 0$ in our coordinates, Eq (2.18). An outward normal is $\omega = -dz$, and consequently the outward unit-normal for this boundary reads $n_A = \omega_A / \sqrt{\omega_A \omega_B G^{AB}}$. Noting that it is perpendicular to the future directed unit vector field u^A —defined above Eq. (C.3)—it follows that

$$u^B \nabla_B (n_A u^A) = 0 = u^A u^B \nabla_B n_A + n^A u^B \nabla_B u_A = u^A u^B K_{AB} + n^A a_A, \quad (\text{C.14})$$

since the extrinsic curvature is $K_{AB} = h_A^C h_B^D \nabla_C n_D$. Hence, at the asymptotic boundary

$$\frac{1}{\zeta^2} \zeta_B n_A \nabla^A \zeta^B = -\frac{1}{Z^2} \zeta_B n_A \nabla^A \zeta^B = \frac{1}{Z} n_A \nabla^A (Z) = n_A a^A = -u^A u^B K_{AB} = K_t^t, \quad (\text{C.15})$$

where we used Eqs. (C.2), (C.3) and (C.14). In the last equality we particularized the result to our choice of coordinates. We conclude that the integral at this boundary is

$$I_\infty = -\frac{1}{\kappa_5^2} \int d^4x \sqrt{-h} K_t^t. \quad (\text{C.16})$$

This integral is divergent, but its divergences will be canceled by the GHY term and the conunterterms, Eqs. (B.4) and (B.5).

On the other hand, the horizon lies at the constant $z = z_{\text{H}}$ slice. The corresponding outward normal is $\lambda = +dz$, with outward unit-normal given by $m_A = \lambda_A / \sqrt{\lambda_B \lambda_C G^{BC}}$. The horizon contribution is then

$$I_{\text{H}} = -\frac{1}{\kappa_5^2} \lim_{z \rightarrow z_{\text{H}}} \int \frac{\zeta_B}{\zeta^2} \nabla^A \zeta^B d\Sigma_A^{(\text{H})} = -\frac{1}{\kappa_5^2} \lim_{z \rightarrow z_{\text{H}}} \int \frac{\zeta_B}{\zeta^2} \nabla^A \zeta^B m_A \sqrt{|h^{(\text{H})}|} d^4y \quad (\text{C.17})$$

In coordinates for which G_{MN} is block diagonal, such as the ones used in Eq. (2.18), the square root of the determinant can be written as $\sqrt{|h^{(\text{H})}|} = \sqrt{-G_{tt}} \cdot \sqrt{q^{(\text{H})}}$, and the integral at the horizon becomes

$$I_{\text{H}} = \frac{1}{\kappa_5^2} \lim_{z \rightarrow z_{\text{H}}} \int \left(-\frac{\zeta_B}{\zeta^2} \nabla^A \zeta^B m_A \sqrt{-G_{tt}} \right) \times \sqrt{|q^{(\text{H})}|} dt d^3y. \quad (\text{C.18})$$

When the limit is taken, the piece inside the parenthesis equals the surface gravity, κ_{H} . Secretly, this is because ζ^A is the horizon generator, and m_A is perpendicular to it. In addition, the left over square root gives the horizon area density. Hence,

$$I_{\text{H}} = \frac{\kappa_{\text{H}}}{\kappa_5^2} \int \sqrt{|q^{(\text{H})}|} dt d^3y = TS \int dt. \quad (\text{C.19})$$

Putting Eqs. (C.16) and (C.19) together we obtain

$$I_{\text{ren}} = \frac{1}{\kappa_5^2} \int d^4x \sqrt{-h} \left(-K_t^t + K + \frac{2}{L} \left(-\frac{3}{2} - \frac{\phi^2}{2} + \lambda_4 \phi^4 \right) \right) + TS \int dt. \quad (\text{C.20})$$

Now we perform a Wick rotation $t \mapsto -i\tau$ in Eq. (C.20) to obtain the Euclidean action, $I_{\text{ren}}^{(\text{E})} = -iI_{\text{ren}}|_{t \mapsto -i\tau}$. After integrating the compact Euclidean time coordinate $\tau \in (0, \beta)$,

$$I_{\text{ren}}^{(\text{E})} = -\frac{\beta}{\kappa_5^2} \int d^3x \sqrt{h_E} \left(-K_t^t + K + \frac{2}{L} \left(-\frac{3}{2} - \frac{\phi^2}{2} + \lambda_4 \phi^4 \right) \right) - \beta TS. \quad (\text{C.21})$$

From this we obtain an expression for the free energy, since $I_{\text{ren}}^{(\text{E})} = \beta F$. Evaluating the integrand in Eq. (C.21) using the UV expansions (2.12) and (2.21), we discover that the first term is just the energy, given in Eq. (2.33). In conclusion, we obtain

$$F = E - TS. \quad (\text{C.22})$$

D Calculation of the two-point function

In order to compute the two-point function we perturb the homogeneous solution, introducing fluctuations of the metric and the scalar. It is convenient to work we do in Eddington-Finkelstein coordinates as in Ref. [98],

$$ds^2 = -F(u)dt^2 + 2H(u)dudt + S(u)^2(dx_1^2 + dx_2^2 + dx_3^2). \quad (\text{D.1})$$

This ansatz for the metric is related to Eq. (2.6) via

$$H(u)du = \frac{L^2}{z^2} f(z)^{\frac{1}{2}} dz, \quad F(u) = \frac{L^2}{z^2} f(z), \quad S(u) = \frac{L}{z} g(z)^{\frac{1}{2}}. \quad (\text{D.2})$$

Generically, the fluctuations take the form

$$G_{\mu\nu} \mapsto G_{\mu\nu} + \epsilon h_{\mu\nu}(t, \vec{x}, u) + O(\epsilon^2), \quad \phi \mapsto \phi + \epsilon \delta\phi(t, \vec{x}, u) + O(\epsilon^2), \quad (\text{D.3})$$

but we will be interested in plane wave perturbations, and so we take the simplified ansatz

$$h_{\mu\nu}(t, x_1, u) = e^{-i(\omega t - qx_1)} h_{\mu\nu}(u), \quad \delta\phi(t, x_1, u) = e^{-i(\omega t - qx_1)} \delta\phi(u). \quad (\text{D.4})$$

In our case, only scalar perturbations matter for the computation of the effective action. The two relevant gauge invariant combinations are⁷

$$Z_2 = h_{tt} + 2\frac{\omega}{q} h_{tx} + \frac{\omega^2}{q^2} h_{xx} + \left(-\frac{\omega^2}{q^2} + \frac{F'}{2SS'} \right) h, \quad Z_\phi = \delta\phi - \frac{\phi'}{2SS'} h, \quad (\text{D.5})$$

with $h = (h_{22} + h_{33})/2$ and primes here indicating derivatives with respect to u . Since we are interested in constructing critical bubbles, which are static configurations, from now on we set $\omega = 0$. The solutions then approach the boundary of spacetime as

$$\begin{aligned} Z_\phi &= a_1 z + \left(a_3 + \left(\frac{a_1 q^2}{2} - b_0 \frac{\Lambda}{12L^2} \right) \log z \right) z^3 + O(z^4) . \\ Z_2 &= \frac{1}{z^2} \left(b_0 - \frac{1}{12} b_0 (3q^2 + 4\Lambda^2) z^2 + \left(b_4 - \frac{b_0 q^2}{48} (3q^2 + 4\Lambda^2) \log(z) \right) z^4 + O(z^6) \right) . \end{aligned} \quad (\text{D.6})$$

We emphasize that Λ is the coupling, given by the leading order in the background scalar field, see Eq. (2.12).

Since the kinetic term appears as a gradient expansion of the fluctuations, we focus on the limit of small momenta, $q \rightarrow 0$. Therefore we expand

$$Z_2(z) = Z_2^{(0)}(z) + q^2 Z_2^{(2)}(z) + O(q^3), \quad Z_\phi(z) = Z_\phi^{(0)}(z) + q^2 Z_\phi^{(2)}(z) + O(q^3). \quad (\text{D.7})$$

Later, we will see that it is precisely in taking this small q limit that some subtleties arise. Let us for now relate Eqs. (D.6) and (D.7) by substituting the latter into the equations for the fluctuations. By doing so, we find a system of four second order ODEs for $Z_i^{(0)}(z)$ and $Z_i^{(2)}(z)$ which does not depend on q . Close to the boundary the solution for each function in the momentum expansion becomes

$$\begin{aligned} Z_\phi^{(0)}(z) &= a_{1,0} z + a_{3,0} z^3 + O(z^4), \\ Z_2^{(0)}(z) &= \frac{1}{z^2} \left(b_{0,0} - \frac{b_{0,0}}{3} \Lambda^2 z^2 + b_{4,0} z^4 + O(z^5) \right), \\ Z_\phi^{(2)}(z) &= a_{1,2} z + \left(a_{3,2} + \left(\frac{a_{1,0}}{2} - \frac{b_{0,0} \Lambda}{12L^2} \right) \log(z) \right) z^3 + O(z^4), \\ Z_2^{(2)}(z) &= \frac{1}{z^2} \left(b_{0,2} - \frac{1}{12} z^2 (4\Lambda^2 b_{0,2} + 3b_{0,0}) + \frac{1}{12} z^4 (12b_{0,4} - b_{0,0} \Lambda^2 \log(z)) + O(z^5) \right), \end{aligned} \quad (\text{D.8})$$

⁷Note that, compared to [98], $Z_2|_{\text{there}} = q^2 Z_2|_{\text{here}}$.

Note that $a_i = a_{i,0} + a_{i,2}q^2 + O(q^4)$, with $i = 1, 3$; and $b_i = b_{i,0} + b_{i,2}q^2 + O(q^4)$ with $i = 0, 4$.

Because we are not varying the boundary metric, we set $b_0 = b_{0,0} = b_{2,0} = 0$. The two point function is now nicely given in terms of the formula obtained from holographic renormalization, Eq. (B.9), which in this case becomes

$$\delta\langle\mathcal{O}\rangle = \langle\mathcal{O}\rangle - \langle\mathcal{O}\rangle|_{\epsilon=0} = -\frac{\epsilon}{12}e^{iqx_1} \left(8 \left(a_1 \Lambda^2 (18\lambda_4 + 1) + 3a_3 \right) + 3(4\alpha - 1)a_1 q^2 \right), \quad (\text{D.9})$$

$$\delta J = \phi_{(0)}(x) - \Lambda = a_1 \epsilon e^{iqx_1}.$$

Note the explicit appearance of α , which boils down to the fact that the source for the leading order of the scalar $\phi_{(0)}(x)$ is no longer constant and, consequently, $\psi_{(2)} \neq 0$, see Eq. (B.1).

From the variations in Eq. (D.9) we can easily compute the two point function at the homogeneous equilibrium states, i.e. the Green's function:

$$\tilde{G}_0 = \langle\mathcal{O}\mathcal{O}\rangle = \frac{\delta\langle\mathcal{O}\rangle}{\delta J} \Big|_{J=0} = -\frac{8(a_1(18\lambda_4 + 1)\Lambda^2 + 3a_3) + 3(4\alpha - 1)a_1 q^2}{12a_1}$$

$$= \left(-\frac{2a_{3,0}}{a_{1,0}} - \frac{2}{3}\Lambda^2(1 + 18\lambda_4) \right) + \left(\frac{1}{4} + \frac{2a_{1,2}a_{3,0}}{a_{1,0}^2} - \frac{2a_{3,2}}{a_{1,0}} - \alpha \right) q^2 + O(q^4). \quad (\text{D.10})$$

The inverse of this two point function is

$$\tilde{G}_0^{-1} = -\frac{3a_{1,0}}{2(3a_{3,0} + a_{1,0}\Lambda^2(1 + 18\lambda_4))} + \frac{9(-8a_{1,2}a_{3,0} + 8a_{1,0}a_{3,2} + a_{1,0}^2(4\alpha - 1))q^2}{16(3a_{3,0} + a_{1,0}\Lambda^2 + 18a_{1,0}\Lambda^2\lambda_4)^2} + O(q^4). \quad (\text{D.11})$$

From Eq. (D.11) we would say that the would-be kinetic term is

$$Z_\alpha(\varphi) = -\frac{9(-8a_{1,2}a_{3,0} + 8a_{1,0}a_{3,2} + a_{1,0}^2(4\alpha - 1))}{16(3a_{3,0} + a_{1,0}\Lambda^2 + 18a_{1,0}\Lambda^2\lambda_4)^2}. \quad (\text{D.12})$$

The actual scheme-independent kinetic term is obtained from the pole of the correlator P_0 . Using the expression for the second derivative of the potential in Eq. (D.11), the kinetic term is related to the pole as

$$Z(\varphi) = -\frac{1}{R_0} = -\frac{3a_{1,0}}{2(3a_{3,0} + a_{1,0}\Lambda^2(1 + 18\lambda_4))} \times P_0^{-1}. \quad (\text{D.13})$$

References

- [1] A. D. Linde, *Phase Transitions in Gauge Theories and Cosmology*, *Rept. Prog. Phys.* **42** (1979) 389.
- [2] T. W. B. Kibble, *Some Implications of a Cosmological Phase Transition*, *Phys. Rept.* **67** (1980) 183.
- [3] K. Enqvist, J. Ignatius, K. Kajantie and K. Rummukainen, *Nucleation and bubble growth in a first order cosmological electroweak phase transition*, *Phys. Rev. D* **45** (1992) 3415.

- [4] A. Mazumdar and G. White, *Review of cosmic phase transitions: their significance and experimental signatures*, *Rept. Prog. Phys.* **82** (2019) 076901 [[1811.01948](#)].
- [5] M. B. Hindmarsh, M. Lüben, J. Lumma and M. Pauly, *Phase transitions in the early universe*, *SciPost Phys. Lect. Notes* **24** (2021) 1 [[2008.09136](#)].
- [6] C. e. a. Caprini, *Detecting gravitational waves from cosmological phase transitions with LISA: an update*, *JCAP* **1911** (2019) 017 [[1906.09244](#)].
- [7] V. A. Kuzmin, V. A. Rubakov and M. E. Shaposhnikov, *On the Anomalous Electroweak Baryon Number Nonconservation in the Early Universe*, *Phys. Lett. B* **155** (1985) 36.
- [8] M. E. Shaposhnikov, *Baryon Asymmetry of the Universe in Standard Electroweak Theory*, *Nucl. Phys. B* **287** (1987) 757.
- [9] L. D. McLerran, M. E. Shaposhnikov, N. Turok and M. B. Voloshin, *Why the baryon asymmetry of the universe is approximately 10^{-10}* , *Phys. Lett. B* **256** (1991) 451.
- [10] G. R. Farrar and M. E. Shaposhnikov, *Baryon asymmetry of the universe in the minimal Standard Model*, *Phys. Rev. Lett.* **70** (1993) 2833 [[hep-ph/9305274](#)].
- [11] V. A. Rubakov and M. E. Shaposhnikov, *Electroweak baryon number nonconservation in the early universe and in high-energy collisions*, *Usp. Fiz. Nauk* **166** (1996) 493 [[hep-ph/9603208](#)].
- [12] E. Witten, *Cosmic Separation of Phases*, *Phys. Rev. D* **30** (1984) 272.
- [13] C. J. Hogan, *Gravitational radiation from cosmological phase transitions*, *Mon. Not. Roy. Astron. Soc.* **218** (1986) 629.
- [14] A. Kosowsky, M. S. Turner and R. Watkins, *Gravitational radiation from colliding vacuum bubbles*, *Phys. Rev. D* **45** (1992) 4514.
- [15] A. Kosowsky and M. S. Turner, *Gravitational radiation from colliding vacuum bubbles: envelope approximation to many bubble collisions*, *Phys. Rev. D* **47** (1993) 4372 [[astro-ph/9211004](#)].
- [16] M. Kamionkowski, A. Kosowsky and M. S. Turner, *Gravitational radiation from first-order phase transitions*, *Phys. Rev. D* **49** (1994) 2837 [[astro-ph/9310044](#)].
- [17] C. Caprini, R. Durrer and G. Servant, *The stochastic gravitational wave background from turbulence and magnetic fields generated by a first-order phase transition*, *JCAP* **12** (2009) 024 [[0909.0622](#)].
- [18] C. Caprini, M. Hindmarsh, S. J. Huber, T. Konstandin, J. Kozaczuk, G. Nardini et al., *Science with the space-based interferometer eLISA. II: Gravitational waves from cosmological phase transitions*, *JCAP* **04** (2016) 001 [[1512.06239](#)].
- [19] M. Hindmarsh, S. J. Huber, K. Rummukainen and D. J. Weir, *Gravitational waves from the sound of a first-order phase transition*, *Phys. Rev. Lett.* **112** (2014) 041301 [[1304.2433](#)].
- [20] M. Hindmarsh, S. J. Huber, K. Rummukainen and D. J. Weir, *Numerical simulations of acoustically generated gravitational waves at a first order phase transition*, *Phys. Rev. D* **92** (2015) 123009 [[1504.03291](#)].
- [21] T. W. B. Kibble, *Topology of cosmic domains and strings*, *J. Phys. A* **9** (1976) 1387.
- [22] W. H. Zurek, *Cosmological Experiments in Superfluid Helium?*, *Nature* **317** (1985) 505.

[23] A. Rajantie, *Phase transitions in the early universe and defect formation*, in *COSLAB Workshop on Cosmological Phase Transitions and Topological Defects*, 2003, [hep-ph/0311262](#).

[24] M. Kawasaki, K. Saikawa and T. Sekiguchi, *Axion dark matter from topological defects*, *Phys. Rev. D* **91** (2015) 065014 [[1412.0789](#)].

[25] T. Vachaspati, *Kinks and Domain Walls: An Introduction to Classical and Quantum Solitons*. Cambridge University Press, 2010, [10.1017/CBO9780511535129](#).

[26] N. A. Gentile, M. B. Aufderheide, G. J. Mathews, F. D. Swesty and G. M. Fuller, *The QCD phase transition and supernova core collapse*, *Astrophys. J.* **414** (1993) 701.

[27] D. K. Hong, S. D. H. Hsu and F. Sannino, *Supernovae, hypernovae and color superconductivity*, *Phys. Lett. B* **516** (2001) 362 [[hep-ph/0107017](#)].

[28] T. Fischer, I. Sagert, G. Pagliara, M. Hempel, J. Schaffner-Bielich, T. Rauscher et al., *Core-collapse supernova explosions triggered by a quark-hadron phase transition during the early post-bounce phase*, *Astrophys. J. Suppl.* **194** (2011) 39 [[1011.3409](#)].

[29] I. Sagert, T. Fischer, M. Hempel, G. Pagliara, J. Schaffner-Bielich, T. Rauscher et al., *Strange quark matter in core-collapse supernovae*, *Acta Phys. Polon. B Proc. Suppl.* **5** (2012) 791 [[1112.6328](#)].

[30] T. Fischer et al., *Core collapse supernovae in the QCD phase diagram*, *Phys. Atom. Nucl.* **75** (2012) 613 [[1103.3004](#)].

[31] N. Nishimura, T. Fischer, F.-K. Thielemann, C. Frohlich, M. Hempel, R. Kappeli et al., *Nucleosynthesis in core-collapse supernova explosions triggered by a quark-hadron phase transition*, *Astrophys. J.* **758** (2012) 9 [[1112.5684](#)].

[32] N. K. Glendenning, *First order phase transitions with more than one conserved charge: Consequences for neutron stars*, *Phys. Rev. D* **46** (1992) 1274.

[33] M. G. Alford, D. Blaschke, A. Drago, T. Klähn, G. Pagliara and J. Schaffner-Bielich, *Quark matter in compact stars?*, *Nature* **445** (2007) 7 [[astro-ph/0606524](#)].

[34] A. Bauswein, S. Blacker, V. Vijayan, N. Stergioulas, K. Chatzioannou, J. A. Clark et al., *Identifying a first-order phase transition in neutron star mergers through gravitational waves*, *Phys. Rev. Lett.* **122** (2019) 061102 [[1809.01116](#)].

[35] E. R. Most, L. R. Weih, L. Rezzolla and J. Schaffner-Bielich, *New constraints on radii and tidal deformabilities of neutron stars from GW170817*, *Phys. Rev. Lett.* **120** (2018) 261103 [[1803.00549](#)].

[36] E. R. Most, L. J. Papenfort, V. Dexheimer, M. Hanauske, S. Schramm, H. Stöcker et al., *Signatures of quark-hadron phase transitions in general-relativistic neutron-star mergers*, *Phys. Rev. Lett.* **122** (2019) 061101 [[1807.03684](#)].

[37] C. Ecker, M. Järvinen, G. Nijs and W. van der Schee, *Gravitational waves from holographic neutron star mergers*, *Phys. Rev. D* **101** (2020) 103006 [[1908.03213](#)].

[38] A. Prakash, D. Radice, D. Logoteta, A. Perego, V. Nedora, I. Bombaci et al., *Signatures of deconfined quark phases in binary neutron star mergers*, *Phys. Rev. D* **104** (2021) 083029 [[2106.07885](#)].

[39] L. R. Weih, M. Hanauske and L. Rezzolla, *Postmerger Gravitational-Wave Signatures of Phase Transitions in Binary Mergers*, *Phys. Rev. Lett.* **124** (2020) 171103 [[1912.09340](#)].

[40] S. Tootle, C. Ecker, K. Topolski, T. Demircik, M. Järvinen and L. Rezzolla, *Quark formation and phenomenology in binary neutron-star mergers using V-QCD*, *SciPost Phys.* **13** (2022) 109 [[2205.05691](#)].

[41] J. Casalderrey-Solana, D. Mateos and M. Sanchez-Garitaonandia, *Mega-Hertz Gravitational Waves from Neutron Star Mergers*, [2210.03171](#).

[42] A. D. Linde, *Decay of the False Vacuum at Finite Temperature*, *Nucl. Phys. B* **216** (1983) 421.

[43] S. R. Coleman, *The Fate of the False Vacuum. 1. Semiclassical Theory*, *Phys. Rev. D* **15** (1977) 2929.

[44] A. G. Cohen, D. B. Kaplan and A. E. Nelson, *Progress in electroweak baryogenesis*, *Ann. Rev. Nucl. Part. Sci.* **43** (1993) 27 [[hep-ph/9302210](#)].

[45] D. E. Morrissey and M. J. Ramsey-Musolf, *Electroweak baryogenesis*, *New J. Phys.* **14** (2012) 125003 [[1206.2942](#)].

[46] M. Joyce, T. Prokopec and N. Turok, *Nonlocal electroweak baryogenesis. Part 2: The Classical regime*, *Phys. Rev. D* **53** (1996) 2958 [[hep-ph/9410281](#)].

[47] J. M. Maldacena, *The Large N limit of superconformal field theories and supergravity*, *Adv. Theor. Math. Phys.* **2** (1998) 231 [[hep-th/9711200](#)].

[48] E. Witten, *Anti-de Sitter space and holography*, *Adv. Theor. Math. Phys.* **2** (1998) 253 [[hep-th/9802150](#)].

[49] S. S. Gubser, I. R. Klebanov and A. M. Polyakov, *Gauge theory correlators from noncritical string theory*, *Phys. Lett. B* **428** (1998) 105 [[hep-th/9802109](#)].

[50] M. P. Heller and R. A. Janik, *Viscous hydrodynamics relaxation time from AdS/CFT*, *Phys. Rev. D* **76** (2007) 025027 [[hep-th/0703243](#)].

[51] P. M. Chesler and L. G. Yaffe, *The Wake of a quark moving through a strongly-coupled plasma*, *Phys. Rev. Lett.* **99** (2007) 152001 [[0706.0368](#)].

[52] P. M. Chesler and L. G. Yaffe, *The Stress-energy tensor of a quark moving through a strongly-coupled $N=4$ supersymmetric Yang-Mills plasma: Comparing hydrodynamics and AdS/CFT*, *Phys. Rev. D* **78** (2008) 045013 [[0712.0050](#)].

[53] P. M. Chesler, K. Jensen, A. Karch and L. G. Yaffe, *Light quark energy loss in strongly-coupled $N = 4$ supersymmetric Yang-Mills plasma*, *Phys. Rev. D* **79** (2009) 125015 [[0810.1985](#)].

[54] P. M. Chesler and L. G. Yaffe, *Boost invariant flow, black hole formation, and far-from-equilibrium dynamics in $N = 4$ supersymmetric Yang-Mills theory*, *Phys. Rev. D* **82** (2010) 026006 [[0906.4426](#)].

[55] P. M. Chesler and L. G. Yaffe, *Holography and colliding gravitational shock waves in asymptotically AdS_5 spacetime*, *Phys. Rev. Lett.* **106** (2011) 021601 [[1011.3562](#)].

[56] M. P. Heller, R. A. Janik and P. Witaszczyk, *The characteristics of thermalization of boost-invariant plasma from holography*, *Phys. Rev. Lett.* **108** (2012) 201602 [[1103.3452](#)].

[57] J. Casalderrey-Solana, M. P. Heller, D. Mateos and W. van der Schee, *From full stopping to transparency in a holographic model of heavy ion collisions*, *Phys. Rev. Lett.* **111** (2013) 181601 [[1305.4919](#)].

[58] M. Attems, Y. Bea, J. Casalderrey-Solana, D. Mateos, M. Triana and M. Zilhão, *Phase Transitions, Inhomogeneous Horizons and Second-Order Hydrodynamics*, *JHEP* **06** (2017) 129 [[1703.02948](#)].

[59] R. A. Janik, J. Jankowski and H. Soltanpanahi, *Real-Time dynamics and phase separation in a holographic first order phase transition*, *Phys. Rev. Lett.* **119** (2017) 261601 [[1704.05387](#)].

[60] M. Attems, Y. Bea, J. Casalderrey-Solana, D. Mateos, M. Triana and M. Zilhão, *Holographic Collisions across a Phase Transition*, *Phys. Rev. Lett.* **121** (2018) 261601 [[1807.05175](#)].

[61] M. Attems, Y. Bea, J. Casalderrey-Solana, D. Mateos and M. Zilhão, *Dynamics of Phase Separation from Holography*, *JHEP* **01** (2020) 106 [[1905.12544](#)].

[62] L. Bellantuono, R. A. Janik, J. Jankowski and H. Soltanpanahi, *Dynamics near a first order phase transition*, *JHEP* **10** (2019) 146 [[1906.00061](#)].

[63] Y. Bea, J. Casalderrey-Solana, T. Giannakopoulos, A. Jansen, S. Krippendorf, D. Mateos et al., *Spinodal Gravitational Waves*, *JHEP* **11** (2025) 093 [[2112.15478](#)].

[64] R. A. Janik, M. Jarvinen and J. Sonnenschein, *A simple description of holographic domain walls in confining theories — extended hydrodynamics*, *JHEP* **09** (2021) 129 [[2106.02642](#)].

[65] Y. Bea, J. Casalderrey-Solana, T. Giannakopoulos, D. Mateos, M. Sanchez-Garitaonandia and M. Zilhão, *Bubble wall velocity from holography*, *Phys. Rev. D* **104** (2021) L121903 [[2104.05708](#)].

[66] F. Bigazzi, A. Caddeo, T. Canneti and A. L. Cotrone, *Bubble wall velocity at strong coupling*, *JHEP* **08** (2021) 090 [[2104.12817](#)].

[67] Y. Bea, J. Casalderrey-Solana, T. Giannakopoulos, A. Jansen, D. Mateos, M. Sanchez-Garitaonandia et al., *Holographic bubbles with Jecco: expanding, collapsing and critical*, *JHEP* **09** (2022) 008 [[2202.10503](#)].

[68] Y. Bea, M. Giliberti, D. Mateos, M. Sanchez-Garitaonandia, A. Serantes and M. Zilhão, *Bubble dynamics in a QCD-like phase diagram*, [2412.09588](#).

[69] F. R. Ares, M. Hindmarsh, C. Hoyos and N. Jokela, *Gravitational waves from a holographic phase transition*, *JHEP* **21** (2020) 100 [[2011.12878](#)].

[70] F. R. Ares, O. Henriksson, M. Hindmarsh, C. Hoyos and N. Jokela, *Gravitational Waves at Strong Coupling from an Effective Action*, *Phys. Rev. Lett.* **128** (2022) 131101 [[2110.14442](#)].

[71] F. R. Ares, O. Henriksson, M. Hindmarsh, C. Hoyos and N. Jokela, *Effective actions and bubble nucleation from holography*, *Phys. Rev. D* **105** (2022) 066020 [[2109.13784](#)].

[72] O. Henriksson, N. Jokela and X. Li, *Testing the effective action approach to bubble nucleation in holography*, [2507.11622](#).

[73] Y. Bea and D. Mateos, *Heating up Exotic RG Flows with Holography*, *JHEP* **08** (2018) 034 [[1805.01806](#)].

[74] Y. Bea, O. J. C. Dias, T. Giannakopoulos, D. Mateos, M. Sanchez-Garitaonandia, J. E. Santos et al., *Crossing a large- N phase transition at finite volume*, *JHEP* **02** (2021) 061 [[2007.06467](#)].

[75] A. F. Faedo, C. Hoyos, M. Piai, R. Rodgers and J. G. Subils, *Light holographic dilatons near critical points*, *Phys. Rev. D* **110** (2024) 126017 [[2406.04974](#)].

[76] M. Headrick, S. Kitchen and T. Wiseman, *A New approach to static numerical relativity, and its application to Kaluza-Klein black holes*, *Class. Quant. Grav.* **27** (2010) 035002 [[0905.1822](#)].

[77] T. Wiseman, *Numerical construction of static and stationary black holes*, pp. 233–270. 2012. [1107.5513](#).

[78] O. J. C. Dias, J. E. Santos and B. Way, *Numerical Methods for Finding Stationary Gravitational Solutions*, *Class. Quant. Grav.* **33** (2016) 133001 [[1510.02804](#)].

[79] P. Figueras, J. Lucietti and T. Wiseman, *Ricci solitons, Ricci flow, and strongly coupled CFT in the Schwarzschild Unruh or Boulware vacua*, *Class. Quant. Grav.* **28** (2011) 215018 [[1104.4489](#)].

[80] P. Figueras and T. Wiseman, *On the existence of stationary Ricci solitons*, *Class. Quant. Grav.* **34** (2017) 145007 [[1610.06178](#)].

[81] M. Laine and A. Vuorinen, *Basics of Thermal Field Theory*, vol. 925. Springer, 2016, 10.1007/978-3-319-31933-9, [[1701.01554](#)].

[82] M. Henningson and K. Skenderis, *The Holographic Weyl anomaly*, *JHEP* **07** (1998) 023 [[hep-th/9806087](#)].

[83] V. Balasubramanian and P. Kraus, *A Stress tensor for Anti-de Sitter gravity*, *Commun. Math. Phys.* **208** (1999) 413 [[hep-th/9902121](#)].

[84] S. de Haro, S. N. Solodukhin and K. Skenderis, *Holographic reconstruction of space-time and renormalization in the AdS / CFT correspondence*, *Commun. Math. Phys.* **217** (2001) 595 [[hep-th/0002230](#)].

[85] K. Skenderis, *Lecture notes on holographic renormalization*, *Class. Quant. Grav.* **19** (2002) 5849 [[hep-th/0209067](#)].

[86] S. Bhattacharyya, V. E. Hubeny, S. Minwalla and M. Rangamani, *Nonlinear Fluid Dynamics from Gravity*, *JHEP* **02** (2008) 045 [[0712.2456](#)].

[87] B. Lucini, M. Teper and U. Wenger, *Properties of the deconfining phase transition in $SU(N)$ gauge theories*, *JHEP* **02** (2005) 033 [[hep-lat/0502003](#)].

[88] A. Salami, T. Rindlisbacher and K. Rummukainen, *The confined-deconfined surface tension in $SU(N)$ gauge theories at large N* , *PoS LATTICE2024* (2025) 406 [[2502.01396](#)].

[89] P. Agrawal, G. R. Kane, V. Loladze and J. March-Russell, *A Prediction for Maximum Supercooling in $SU(N)$ Confinement Transition*, [2508.10091](#).

[90] J. Casalderrey-Solana and P. Zaera Espuny, *unpublished*, 2023.

[91] D. Cutting, E. G. Escartin, M. Hindmarsh and D. J. Weir, *Gravitational waves from vacuum first order phase transitions II: from thin to thick walls*, *Phys. Rev. D* **103** (2021) 023531 [[2005.13537](#)].

[92] F. Denef, S. A. Hartnoll and S. Sachdev, *Black hole determinants and quasinormal modes*, *Class. Quant. Grav.* **27** (2010) 125001 [[0908.2657](#)].

[93] A. Krikun, *Numerical Solution of the Boundary Value Problems for Partial Differential Equations. Crash course for holographer*, 1, 2018, [1801.01483](#).

[94] M. Bianchi, D. Z. Freedman and K. Skenderis, *How to go with an RG flow*, *JHEP* **08** (2001) 041 [[hep-th/0105276](#)].

- [95] M. Bianchi, D. Z. Freedman and K. Skenderis, *Holographic renormalization*, *Nucl. Phys. B* **631** (2002) 159 [[hep-th/0112119](#)].
- [96] C. Ecker, E. Kiritsis and W. van der Schee, *Dynamical Inflaton Coupled to Strongly Interacting Matter*, *Phys. Rev. Lett.* **130** (2023) 251001 [[2302.06618](#)].
- [97] I. Papadimitriou, *Holographic Renormalization of general dilaton-axion gravity*, *JHEP* **08** (2011) 119 [[1106.4826](#)].
- [98] A. Jansen, *Overdamped modes in Schwarzschild-de Sitter and a Mathematica package for the numerical computation of quasinormal modes*, *Eur. Phys. J. Plus* **132** (2017) 546 [[1709.09178](#)].